

1 **Testing the magnetotail configuration based on**
2 **observations of low altitude isotropic boundaries**
3 **during quiet times**

R. Ilie¹, N. Ganushkina^{1,2}, G. Toth¹, S. Dubyagin², M. W. Liemohn¹

R. Ilie, University of Michigan, Ann Arbor, MI, 48109, USA. (rilie@umich.edu)

N. Ganushkina, University of Michigan, Ann Arbor, MI 48109, USA.

G. Toth, University of Michigan, Ann Arbor, MI 48109, USA.

S. Dubyagin, Finish Meteorological Institute, Helsinki, Finland

M.W. Liemohn, University of Michigan, Ann Arbor, MI 48109, USA.

¹University of Michigan, MI, USA.

²Finish Meteorological Institute, Helsinki,
Finland

This is the author manuscript accepted for publication and has undergone full peer review but has not been through the copyediting, typesetting, pagination and proofreading process, which may lead to differences between this version and the Version of Record. Please cite this article as doi:

10.1029/2015JA021858

December 10, 2015, 8:09am

D R A F T

Abstract.

We investigate the configuration of the geomagnetic field on the nightside magnetosphere during a quiet time interval based on NOAA/POES MEPED measurements in combination with numerical simulations of the global terrestrial magnetosphere using the Space Weather Modeling Framework (SWMF). Measurements from the NOAA/POES MEPED low-altitude data sets provide the locations of isotropic boundaries; those are used to extract information regarding the field structure in the source regions in the magnetosphere.

In order to evaluate adiabaticity and mapping accuracy, which is mainly controlled by the ratio between the radius of curvature and the particle's Larmor radius, we tested the threshold condition for strong pitch angle scattering based on the MHD magnetic field solution. The magnetic field configuration is represented by the model with high accuracy, as suggested by the high correlation coefficients and very low normalized root mean square errors between the observed and the modeled magnetic field. The scattering criterion, based on the values of $k = \frac{R_c}{\rho}$ ratio at the crossings of magnetic field lines, associated with isotropic boundaries, with the minimum \mathbf{B} surface, predicts a critical value of $k_{CR} \sim 33$. This means that, in the absence of other scattering mechanisms, the strong pitch angle scattering takes place whenever the Larmor radius is ~ 33 times smaller than the radius of curvature of the magnetic field, as predicted by the Space Weather Modeling Framework.

1. Introduction

27 Determining the geometry of the Earth's magnetic field under various solar wind and
28 interplanetary magnetic field (IMF) conditions is crucial for understanding the connections
29 between ionospheric and auroral features and magnetospheric phenomena. Knowledge of
30 the configuration of the magnetic field lines is required in order to understand the magnetic
31 mapping in different conditions and between different regions of the near-Earth space.

32 Isotropic boundaries (IBs) have been proposed as proxies to estimate the degree of mag-
33 netic field stretching in the magnetotail [e.g. *Sergeev et al.*, 1993; *Sergeev and Gvozdevsky*,
34 1995; *Meurant et al.*, 2007] and have been the subject of numerous studies [e.g. *Sergeev*
35 *and Tsyganenko*, 1982; *Tsyganenko*, 1982; *Sergeev et al.*, 1983; *Buechner and Zelenyi*,
36 1987; *Sergeev et al.*, 1994; *Delcourt et al.*, 1996; *Donovan et al.*, 2003b; *Ganushkina et al.*,
37 2005; *Lvova et al.*, 2005; *Kubyshkina et al.*, 2009; *Dubyagin et al.*, 2013]. They are in-
38 terpreted as the separation between the adiabatic and stochastic particle motion in the
39 tail current sheet since they correspond to locations where the locally trapped and the
40 precipitated fluxes of energetic particles are comparable [*Fritz*, 1970] and characterize the
41 transition from weak precipitation rate to isotropic precipitation in the high latitude re-
42 gion. In the regions where the magnetic field line curvature becomes comparable to the
43 particle gyroradius, significant pitch angle scattering occurs [*Tsyganenko*, 1982; *Buechner*
44 *and Zelenyi*, 1987; *Delcourt et al.*, 1996]. *Blockx et al.* [2005, 2007] showed that the SI12
45 camera on board the IMAGE spacecraft [*Sandel et al.*, 2000] was an excellent tool to
46 remotely determine the position of the isotropy boundary in the ionosphere, and thus was

47 able to provide a reasonable estimate of the amount of magnetic field stretching in the
48 magnetotail.

49 The isotropic boundary depends only on the equatorial magnetic field and the particle
50 rigidity. The usefulness of the IB location as an indicator of the tail current characteristics
51 was suggested by *Sergeev et al.* [1993], who showed that the measured IB latitude correlates
52 very well with the magnetic field direction measured by GOES satellite at geostationary
53 orbit near the tail current sheet. The magnetic inclination angle in the tail near the
54 current sheet decreases as the measured IB latitude decreases; that is, when the magnetic
55 field becomes more stretched, the IB shifts to lower latitudes. Since by Ampere's law the
56 tangent of the magnetic inclination angle is approximately inversely proportional to the
57 linear current density in the Y_{GSM} -direction, the inverse of the IB latitude reflects the
58 intensity of the current at the near-Earth tail.

59 Isotropic boundaries for ions were observed at all MLTs and all activity conditions. The
60 IB latitudes depend on the particle species, energy, MLT and magnetic activity and for
61 a given species, the higher the energy, the lower the latitude at which the IB is observed
62 [*Sergeev et al.*, 1993; *Sergeev and Gvozdevsky*, 1995]. These boundaries often present
63 dispersion patterns and could potentially be as broad as $\sim 1^\circ$ [*Sergeev et al.*, 2015].
64 However, reversed energy-latitude dispersion patterns also have been observed *Donovan*
65 *et al.* [2003a]. These lower energy ion precipitation boundaries that extend to lower
66 latitude than the higher-energy ion precipitation have been associated with scattering by
67 the electromagnetic ion cyclotron (EMIC) waves. It has been suggested that the scattering
68 due to wave particle interactions is most effective in the plasma tubes extending $\sim 1R_E$

69 earthward from the boundary that separates adiabatic and stochastic particle motion
70 [*Sergeev et al.*, 2015].

71 The location of the IB could also place a lower bound on the mapping of the substorm
72 onset location [*Gilson et al.*, 2011, 2012]. *Sergeev and Gvozdevsky* [1995] derived the so-
73 called MT-index (further developed by *Asikainen et al.* [2010]), from the observed position
74 (latitude and MLT) of the IB of 100 keV protons. This index characterizes the large-scale
75 tailward stretching of the magnetic field lines in the magnetotail at 5-10 R_E distances and
76 it changes approximately linearly with changes of the magnetic field and inclination at
77 the geostationary orbit at midnight. A semi-empirical model derived by *Asikainen et al.*
78 [2010] describes the contributions of the ring, tail, and magnetopause currents to the Dst
79 index parametrized by solar wind and IMF parameters and by the observed IB latitudes.

80 Continuous measurements on NOAA satellites can provide, though indirectly, valu-
81 able information about the dynamics of the magnetotail. The extensive NOAA/POES
82 MEPED low-altitude data sets provide the locations of isotropic boundaries (IB) that
83 are used to learn about particle distributions and field structure in the source regions
84 in the magnetosphere [*Sergeev et al.*, 1993; *Ganushkina et al.*, 2005; *Lvova et al.*, 2005;
85 *Kubyshkina et al.*, 2009].

86 The only way to determine the magnetic field configuration in the entire magnetosphere
87 is to use an existing model. Empirical models such as the most widely used Tsyganenko
88 models [e.g. *Tsyganenko*, 1995, 2002; *Tsyganenko and Sitnov*, 2005] based on tens of years
89 of satellite data, or models based on analytical relations describing the dynamics of differ-
90 ent magnetic field sources dependent on input parameters [*Alexeev et al.*, 2001], provide
91 magnetospheric configurations corresponding to average conditions. Event-oriented mod-

els developed to provide a realistic representation of the magnetospheric magnetic field during geomagnetic storms are most suitable for post-analysis of specific events [*Ganushkina et al.*, 2004, 2010]. A global representation of the magnetic field can also be obtained based on first principles (such as MHD), self consistently coupled numerical models.

For this study, we analyze the NOAA/POES MEPED data during the February 13, 2009 quiet time period, in combination with first principles based simulations with the Space Weather Modeling Framework (SWMF and the models coupled therein [*Tóth et al.*, 2005, 2012]) in order to determine what is the strong scattering threshold condition based on magnetic field representation as described by the SWMF model. That is, we test the conditions when the nightside particle precipitation is dominated by field line curvature scattering of central plasma sheet particles into the loss cone without including wave-particle interactions.

The article is organized as following: In Section 2 and 3 we present an overview of the time interval investigated and the observations of the isotropy boundaries, respectively. Section 4 presents the description of the model while its validation is presented in Section 5. The results of mapping the isotropic boundaries are shown in Sections 6 and 7. Discussion and Conclusions are presented in Sections 8 and 9, respectively.

2. Overview of the quiet time interval: February 13, 2009

We apply our methodology to a 24 hours long quiet time interval, February 13, 2009, which was selected based on the availability of magnetic field observations on the nightside magnetosphere. During this time, magnetic field data was available from the GOES, Cluster, Geotail and THEMIS spacecraft.

113 The initial selection of a quiet time period was prompted by the fact that during undis-
114 turbed conditions, the probability of scattering due to particle interactions with electro-
115 magnetic waves is small since waves are predominantly present in the inner magnetosphere
116 during the periods of the increased magnetospheric activity [*Halford et al.*, 2010; *Braysy*
117 *et al.*, 1998; *Usanova et al.*, 2012]. Furthermore, the effect of inductive and impulsive
118 electric fields that could further accelerate particles is less significant during undisturbed
119 times and the distribution of trapped particles around drift shells is most likely uniform
120 during quiet times.

121 Figure 1 presents the overview of the quiet interval. From top to bottom we show the
122 solar wind parameters from ACE spacecraft, the interplanetary magnetic field, the solar
123 wind number density and temperature, the solar wind velocity vector and the electric
124 field. The following panels show the Cross Polar Cap Potential (CPCP) and Sym-H in-
125 dices throughout this time interval obtained from the OMNI database. The IMF B_z hovers
126 around zero, with a minimum excursion at $-2 nT$, indicative of a weak geoeffectiveness.
127 The solar wind particle density is less than $10 cm^{-3}$ throughout the entire day and the
128 earthward solar wind velocity stays within a nominal range ($\sim 300 km/s$). Also, the
129 CPCP and Sym-H indices are indicative of quiet time since both display very small vari-
130 ations and magnitudes. Furthermore, inspection of ground based observations reveals no
131 wave activity between 2100 and 0300 MLT during this time (*M. Usanova* [2015], personal
132 communication).

3. Observations of Isotropic Boundaries

133 The data from the Medium Energy Proton and Electron Detector (MEPED) onboard
134 the National Oceanic and Atmospheric Administration Polar Orbiting Environment Satel-

135 lites (NOAA/POES) is used to determine IB locations. NOAA/POES satellites have
136 nearly-circular orbits with altitude of 850 km and orbital period of 100 min crossing the
137 auroral oval four times per orbit with just over 14 orbits in a day.

138 The MEPED detector has two telescopes measuring fluxes of trapped particles and
139 those precipitating into the loss cone allowing IB determination. The fluxes are measured
140 in several energy bands for ions (ranging from 30 to 6900 keV), which are assumed to be
141 protons. This study is based on data from the first proton energy band, referred to as P1
142 (30-80 keV) but we also inspected the higher energy channels to exclude the events with
143 anomalous energy-latitude dispersion.

144 We use the IB determination procedure described in detail by *Dubyagin et al.* [2013]
145 which outputs the IB position and the uncertainty interval. Assuming that the satellite
146 moves from the equator to the pole, the equatorial boundary is defined as the poleward-
147 most point where $F^0/F^{90} < 0.5$ and this condition is fulfilled for the 4 preceding points
148 (8s interval); the polar boundary is the first point after the equatorial boundary where
149 $F^0/F^{90} > 0.75$ and $F^0/F^{90} > 0.75$ for 4 subsequent points, where F^0 and F^{90} correspond
150 to the precipitating and the trapped flux, respectively. The IB uncertainty interval was
151 selected so that it ignores brief periods of isotropic or nearly isotropic fluxes at the equa-
152 torial part of auroral oval, which could be caused by a wave-particle interaction scattering
153 mechanism.

154 For the selected event, we obtained the set of IB locations from all NOAA satellites.
155 Figure 2 shows their dependence on magnetic latitude and magnetic local time (MLT)
156 and their evolution with time. During this quiet period, there was very little variation for
157 the location of the isotropic boundaries with magnetic latitude, most of them originating

158 from magnetic latitudes above 60 degrees. Even though they were observed at all MLTs,
159 we only selected the ones that were identified to reside on the night sector between 2100
160 and 0300 MLT. Figure 2 only shows the IB locations considered in this study. In addition,
161 to exclude the possible wave-particle interaction induced IBs, we inspected the IBs for the
162 higher energy channels (P2, P3) to make sure that there is no anomalous energy-latitude
163 dispersion. We focus here only on the observations of isotropic boundaries at times when
164 the THEMIS -A, -D, -E spacecraft were located in the same MLT sector (+/-1h) as the
165 NOAA satellites and at radial distances $r= 7-10 R_E$. To determine the threshold condition
166 for strong pitch angle scattering, requires reasonable knowledge of the local magnetic field.
167 That being said, the comparison with the THEMIS observations, which were on the same
168 MLT sector with the NOAA satellites, ensures that the magnetic field in that region is
169 well described by the model. The event selection was made to maximize the opportunity
170 for such conjugacies, therefore the seven conjugate observations constitute the entire set
171 available at this time and these observations are summarized in Table 1.

4. Methodology: Model Specifications

172 The numerical simulations presented here were performed using the Space Weather
173 Modeling Framework (SWMF) [Tóth *et al.*, 2005, 2012] developed at University of Michi-
174 gan. This framework is a robust numerical tool for heliophysical simulations, providing
175 a high-performance computational capability to simulate the physics from the solar sur-
176 face to the upper atmosphere of the Earth. It contains numerical modules for numerous
177 physics domains, with a state of the art model solving the physics within each domain.
178 The physical domains included in the simulations presented here are: the Global Mag-

179 netosphere (GM), Ionosphere Electrodynamics (IE) and Inner Magnetosphere (IM). The
180 following is a brief description of each of the components.

4.1. Global Magnetosphere

181 The GM domain is represented by the Block Adaptive Tree Solar-wind-type Roe Upwind
182 Scheme (BATS-R-US) global magneto-hydrodynamic (MHD) model [*Powell et al.*, 1999;
183 *Tóth et al.*, 2012], that solves for the transfer of mass and energy from the solar wind
184 to the magnetosphere. This code solves the semi-relativistic MHD equations [*Gombosi*
185 *et al.*, 2002] with the option to include Hall effect terms [*Tóth et al.*, 2008], multi-fluid
186 equations [*Glocer et al.*, 2009], and anisotropic plasma pressure [*Meng et al.*, 2012]. In the
187 simulations described here, BATS-R-US is configured to solve the three dimensional single
188 fluid MHD equations. This component provides the inner magnetosphere (IM) model the
189 field line volume in the whole IM domain, plasma density and temperature at the outer
190 boundary as well as the field aligned currents strength and location.

4.2. Inner Magnetosphere

191 The Rice Convection Model (RCM) [*Harel et al.*, 1981; *Toffoletto et al.*, 2003], the IM
192 model used for this study, solves the energy-dependent particle flows of hot ions and
193 electrons and describes the dynamic behavior of the inner-magnetospheric particles in
194 terms of isotropic fluids in the near Earth region in the spatial domain bounded by closed
195 magnetic field lines and populated by keV energy particles. The IM component provides
196 the density and pressure along the magnetic field lines and feeds this information to the
197 GM component so that the MHD results are corrected towards the IM results [*De Zeeuw*
198 *et al.*, 2004], while BATS-R-US provides the RCM outer boundary as the dynamic, last

199 closed magnetic field boundary. It has been the predominantly used code for SWMF storm
200 studies [e.g. *Zhang et al.*, 2007; *Ilie et al.*, 2010b, a; *Ganushkina et al.*, 2010; *Liemohn et al.*,
201 2011; *Ilie et al.*, 2010b, a; *Ilie et al.*, 2013, 2015].

4.3. Ionospheric Electrodynamics

202 The two-dimensional electric potential and auroral precipitation patterns are described
203 within this domain. The SWMF uses the ionospheric electrodynamics (IE) model of *Ridley*
204 *and Liemohn* [2002] and *Ridley et al.* [2004] which consists of an electric potential solver
205 and a model of the electron precipitation to calculate the height integrated ionospheric
206 quantities at an altitude of ~ 110 km. Calculations of the conductance pattern and particle
207 precipitation are based on the field-aligned currents information passed from the GM
208 component, while the electric potential is passed both to the IM and converted to velocity
209 at the inner boundary of GM.

4.4. Simulation Setup

210 The message passing between these modules is done self-consistently through couplers
211 inside the SWMF. Each of the models within SWMF has been extensively tested, validated
212 and used for scientific studies of the geospace. It has been used extensively to investigate
213 the near-Earth space environment, investigating storm dynamics [*Zhang et al.*, 2007; *Ilie*
214 *et al.*, 2010b, a; *Ganushkina et al.*, 2010; *Ilie et al.*, 2013], solar wind-magnetosphere energy
215 coupling [*Yu and Ridley*, 2009; *Ilie et al.*, 2010b, a; *Ilie et al.*, 2013], and magnetosphere-
216 ionosphere coupling [*Zhang et al.*, 2007; *Glocer et al.*, 2009; *Ilie et al.*, 2015]. An illustration
217 of the modules and their coupling within the SWMF is presented in Figure 3.

218 The GM inner boundary, located at 2.5 Earth radii (R_E), is set with a passive source
219 term in which the density is kept at a constant value and the radial velocity is set to zero.
220 The value we use in this work (28 cm^{-3}) is the nominal value that has been tested and
221 used in numerous SWMF simulations as the default inner boundary condition. This is
222 further discussed in *Welling and Liemohn* [2014] which suggests that this this boundary
223 condition yields a physically reasonable outflow flux to the magnetosphere.

224 The GM used a Cartesian grid extending from 32 R_E upstream to 224 R_E down-tail,
225 128 R_E in both y and z directions. The grid resolution varies from $1/8 R_E$ in the spherical
226 shell 2.5 to 3.5 R_E close to the body, to 4 R_E near the outer edges of the domain using a
227 total of about 4 million grid cells.

228 The simulation was first ran to reach steady state, using local time stepping for the first
229 2500 iterations with independent local time-stepping within each cell from the BATS-R-
230 US computation domain. This means that each cell uses a time step based on the local
231 numerical stability criteria, allowing the BATS-R-US model to accelerate the convergence
232 towards a steady state. After the steady state is reached, the simulation was allowed to
233 run in the time accurate mode. The coupling frequency of GM with IM is 10 seconds
234 while GM and IE exchange information at every 5 seconds. Note that the model setup
235 does not account for wave particle interactions. However, since during the interval studied
236 here wave activity was not recorded, the models involved are appropriate for the problem
237 investigated.

5. SWMF validation: Magnetic field in the tail

238 During the February 13, 2009, several spacecraft were probing the magnetic field on the
239 nightside magnetosphere (GOES11, GOES12, Cluster1-4, Geotail and THEMIS A-E).

240 These particular satellites were virtually “flown” through the SWMF output, extracting
 241 the MHD parameters at the exact time and location of the spacecraft, therefore one to
 242 one data-model comparison is possible.

243 Since both the radius of curvature and the particle gyroradius, and implicitly the k ratio,
 244 are dependent on the total magnetic field magnitude, we validate the magnetic field model
 245 results by comparing them with the corresponding in situ magnetic field observations
 246 available. Figures 4, 5, 6, 7 show four selective examples for such comparison. In each
 247 figure, the satellite position in GSM coordinates is indicated in the top row and magnetic
 248 field components are presented in the following three rows. The black lines represent in
 249 situ measurements of the magnetic field vector while the red lines show the simulated
 250 values for the same quantities extracted from the model output at the satellite location.
 251 Correlation coefficients between the observed and simulated values of B_x , B_y , B_z are
 252 indicated in each of the corresponding panels.

253 To quantify the SWMF performance we use the correlation coefficient and normalized
 254 root mean squared error (nRMSE) (as defined in Equation 1) between each of the modeled
 255 and the observed magnetic field components.

$$nRMSE = \sqrt{\frac{\sum_i^n (x_i - y_i)^2}{\sum_i^n x_i^2}} \quad (1)$$

256 where x represents the measured value, y represents the simulated value, and n corre-
 257 sponds to the number of data-model pairs used in the calculation. nRMSE ranges from
 258 0, which means that the model is in perfect agreement with the observations, to 1. A
 259 value of 1 indicates that the simulation results are within ± 1 of the measured values
 260 means. Table 2 shows these values for these data-model comparisons. Note that for all

the data-model comparisons the nRMSE scores are well below 0.2. In fact, most of the nRMSE are much smaller than 0.2, indicating that the model results are very close to the observed values for the corresponding parameters and the errors are much smaller than the average magnitude of the observations.

However, this value can be misleading, therefore the nRMSE values must be paired with the correlation coefficients for a proper interpretation of these statistics. The correlation coefficients between the simulated and observed data sets, which measure how well the two sample populations vary together, reveal that the magnetic field configuration is modeled very well by the model, throughout this time period (see Table 2 for the entire matrix). The correlation coefficients are mostly above 0.7, except in the case of THEMIS-B comparison between modeled and observed B_z (not shown here). In this case, the observed field shows noisy excursions around zero while the simulated value is much smoother. By running a moving average (with a window of two minutes) through the THEMIS-B observed values of B_z , the correlation coefficient increases to a ~ 0.7 value.

The nRMSE together with the correlation coefficients analysis indicates that the magnetic field is modeled with high accuracy by the SWMF and the model is capable of capturing the trends within the observations.

6. Mapping of the Isotropic Boundaries

We assume that there exists a robust and always operating pitch angle scattering in the magnetic field regions where the conditions for adiabatic particle motion are violated [Tsyganenko, 1982; Buechner and Zelenyi, 1987; Delcourt et al., 1996]. In particular, if the effective Larmor radius ($\rho = \frac{mv}{qB}$, where m is the particle mass, v is the total particle velocity, q is the particle charge and B is the magnetic field) becomes comparable to the

radius of the field line curvature R_c in the equatorial current sheet ($\frac{1}{R_c} = |(\vec{b} \cdot \nabla)\vec{b}|$, where \vec{b} is the unit vector along the magnetic field direction), then the first adiabatic invariant is violated and pitch-angle scattering occurs, allowing particles to be scattered into the loss cone. The scattering efficiency is controlled by the value of $k = \frac{R_c}{\rho}$, which depends on the current sheet structure and particle parameters, as well as on the required amplitude of the pitch angle change.

Using the magnetic field output from the SWMF, we determine the magnetic field lines for several nightside IBs locations and its crossing in the magnetotail at the surface defined by the minimum magnetic field ($B = B_{min}$) points along the magnetic field line. Please note that this event was selected to maximize the number of conjunctions with various satellites. There were only seven times when one of the available satellites in the region were situated within 1 hour MLT and at distances between 7-10 R_E from the IB NOAA observations. However, there were ~ 40 IBs observations between 2100 and 0300 MLT.

To accomplish this, we define an additional grid inside the MHD domain on which we trace all field lines and find the minimum value of magnetic field for each field line. At the location of minimum \mathbf{B} we extract the MHD model parameters needed to calculate the k ratio. An illustration of this method is presented in Figure 8 which shows a side by side comparison between the magnetic field strength on the minimum \mathbf{B} surface and SM $z = 0$ plane at 0403 UT on February 13th, 2009 in our simulation. Calculation of the k ratio on the minimum \mathbf{B} surface removes previous assumptions relating the magnetic equator with a planar surface (usually SM $z = 0$) as well as symmetry constraints on the geomagnetic field. For comparison purposes, we present here both views. A field line, traced from the observed location of NOAA 18 satellite at this time (Magnetic Latitude:

306 -68.5°, MLT: 22.88), crosses each of the two planes at different values of the magnetic field
 307 (at 7.8 nT on the minimum \mathbf{B} surface vs. 8.1 nT on the $z = 0$ SM plane).

308 At the next step, we calculate the $k = \frac{R_e}{\rho}$ ratio for a 30 keV energy particle in the
 309 magnetotail and whenever an isotropic boundary was observed by one of the NOAA
 310 satellites, we trace a field line from the location of the same satellite and locate its crossing
 311 in the magnetotail at the surfaces defined by the minimum \mathbf{B} and by $z = 0$ in SM
 312 coordinates. The local properties of the total magnetic field at these crossings determine
 313 the conditions when the strong pitch angle scattering can occur.

7. Magnetic field lines for selected IB locations

314 Several isotropic boundaries were determined using the procedure developed and de-
 315 scribed by *Dubyagin et al.* [2013] based on NOAA observations during this time period.
 316 Two representative examples of $k = \frac{R_e}{\rho}$ ratio calculations based on SWMF simulation re-
 317 sults are presented in Figures 9 and Figure 10. Figures 9 shows a comparative view of the
 318 k ratio map for a 30 keV energy ion calculated on the minimum \mathbf{B} surface (left panel) and
 319 SM $z = 0$ plane (right panel) at 0403 UT on February 13th, 2009. At this time, isotropic
 320 boundaries were reported at the location of NOAA 18 corresponding to -68.5 degrees in
 321 magnetic latitude (in the Northern hemisphere) and 22.88 MLT. Therefore, a field line
 322 originating at the satellite location at this time is traced within the simulation domain.
 323 The value of the k ratio at the crossing of this field line with the surface of minimum \mathbf{B} is
 324 2.62 while the value of the k ratio at the field line crossing with SM $z = 0$ plane is 2.65.
 325 Since this is a quiet time interval and the IMF B_z at this time is only slightly negative
 326 but close to 0 nT, the magnetic field is dipole like and the differences between the two
 327 planes on the nightside are only minimal.

328 In the same format as Figure 9, Figure 10 presents the simulation results corresponding
 329 to the 1257 UT time snapshot. At this time NOAA 17, located at -67.01 degrees in
 330 magnetic latitude and 22.94 MLT, was recording similar fluxes of the precipitating and
 331 trapped ion populations, hence an isotropic boundary. In the simulation results, we traced
 332 a field line starting at the location of NOAA 17 at this time and the value of k parameter
 333 at its crossing with the surface of minimum \mathbf{B} is 80.88 while at the crossing with the SM
 334 $z = 0$ plane is 82.90. Again, the difference between values of k on the two surfaces is
 335 small.

336 To further check the model accuracy when resolving the magnetic field solution from
 337 SWMF, we identified several isotropic boundaries for which the magnetic field observations
 338 were available in conjunction with these NOAA auroral oval crossings. That is, we found
 339 several instances when the THEMIS -A, -D, -E spacecraft were located near the NOAA
 340 satellite in the MLT sector (± 1 h) and at $r = 7-10 R_e$, which are summarized in Table
 341 1. This allows us to calculate a relative error parameter, $\Delta B = \frac{B^{modeled} - B^{observed}}{B^{observed}}$, where
 342 $B^{modeled}$ represents the magnetic field predicted by the model, while the $B^{observed}$ represents
 343 its observed counterpart. The timing of the observed and modeled magnetic field, which
 344 corresponds to the time of the IB observation, is specified in Table 1. Figure 11 presents
 345 the dependence of the computed values of $k = \frac{R_c}{\rho}$ ratio on the accuracy parameter ΔB .
 346 Note that in this case, due to the fact that one isotropic boundary could be in conjugacy
 347 with more than one THEMIS observation, the k parameter is a multi-value function.

348 When $\Delta B < 0$, then $B_{model} < B_{obs}$ means that the model underestimates the tail cur-
 349 rents and the model magnetic field line is less stretched than the observed field. Therefore
 350 the $\frac{R_c}{\rho}$ ratio predicted by the model is larger than it should be leading to scattering to

351 occur further down the tail. Conversely, when $\Delta B > 0$ then $B_{model} > B_{obs}$ therefore
 352 the model overestimates the field stretching, meaning that in the model, the scattering
 353 occurs closer to the Earth. The red line in the figure represents a linear fit of these data.
 354 Assuming perfect model prediction, that is $\Delta B = 0$, then the scattering criterion is de-
 355 termined at the intersection of this fit. We find that the model setup used here predicts a
 356 $k = \frac{R_c}{\rho}$ ratio ~ 33 . This value (and our analysis so far) states that, in the absence of other
 357 scattering mechanisms, the strong pitch angle scattering takes place whenever the Larmor
 358 radius is ~ 33 smaller of magnitude of the radius of curvature. However, inspection of
 359 all IBs (no only the ones listed in Table 1) revealed that the value of k varies from low
 360 ($k \sim 2$ in Figure 9) to high ($k \sim 80$ in Figure 10).

8. Discussion

361 The *Sergeev et al.* [1983] study cites a critical value of the k parameter of $k_{CR} = 8$
 362 for strong pitch angle scattering, with other works [e.g. *Sergeev and Tsyganenko*, 1982;
 363 *Delcourt et al.*, 1996] citing a range between 6 and 10 for k_{CR} . However, these studies
 364 assume definitions of k for which the minimum \mathbf{B} is the value at the equator therefore
 365 the radius of curvature R_c and the gyroradius ρ are approximative and only dependent
 366 of the B_z component of the magnetic field. Also, the magnetic field outside the current
 367 sheet is tilted with respect to the equatorial plane by 45° , assuming $B_x = B_z$ outside
 368 the field reversal region. Therefore the choice of $k_{CR} = 8$ could be model dependent and
 369 based on several assumptions involved in the numerical model. In this work, the radius
 370 of curvature and the gyroradius were calculated without any simplifications.

371 The IB latitude can be used as an indicator of total current strength only if there is
 372 no other competing scattering mechanism acting. Wave-particle interactions were long

373 considered to be the main mechanism leading to pitch angle scattering of magnetospheric
374 particles, and the measured particle precipitations were interpreted entirely in terms of
375 this mechanism [e.g. *Hultqvist*, 1979]. Various wave-particle interaction processes can
376 take place in the inner magnetosphere, therefore scattering by fluctuating electromagnetic
377 fields (EMIC waves) could also play a role in pitch angle diffusion since these waves can
378 efficiently scatter the particles in the loss cone [e.g. *Erlandson and Ukhorskiy*, 2001; *Yahnin*
379 *and Yahnina*, 2007]. However, there are some uncertainties in explaining the observed
380 isotropic precipitation of energetic particles in terms of the wave particle interactions
381 mechanism [*Sergeev et al.*, 1993]. First, there is no sufficiently detailed picture of wave
382 characteristics over the vast plasma sheet region where isotropic precipitation is observed.
383 Second, even in cases when there is experimental information about waves, it is often not
384 straightforward to decide whether they are able to produce the strong diffusion required
385 to fill the loss cone isotropically.

386 In addition, wave intensity is in general structured and depends on the activity and
387 certainly on particle fluxes, in sharp contrast to the observed properties of the isotropic
388 precipitation of energetic particles [*Braysy et al.*, 1998; *Halford et al.*, 2010]. *Usanova*
389 *et al.* [2012] reported on the low occurrence rate of EMIC waves on the nightside inner
390 magnetosphere during quiet times. Also, the preferential location for EMIC activity
391 is dayside outer magnetosphere and it peaks during the storm main phase. Although
392 unambiguous determination of the type of the isotropization mechanism from low-altitude
393 observations is not possible, the likelihood that scattering by EMIC waves could lead to
394 particle isotropization during the quiet time interval we selected, is rather low. Inspection
395 of ground based observations reveals no wave activity between 2100 and 0300 MLT during

396 this time (*M. Usanova* [2015], personal communication). In addition, we inspected the
397 energy-latitude dispersion of the IBs (those conjugated with THEMIS-A, -D, -E) to make
398 sure that there were no anomalous dispersion events.

399 In order to evaluate adiabaticity, which is mainly controlled by the ratio between the
400 radius of curvature and the particle's Larmor radius, we tested the threshold condition
401 for strong pitch angle scattering. We found that, in the absence of other scattering
402 mechanisms, the strong pitch angle scattering takes place whenever the Larmor radius
403 is within two orders of magnitude of the radius of curvature of the magnetic field. This
404 means that the k parameter varies in a larger range ($2 < k < 85$) than previous studies
405 suggested. Furthermore, our first-principles based numerical model predicts a critical
406 value of $k_{CR} \sim 33$. Our findings are supported by the high accuracy with which the
407 numerical model, as represented by the high correlation coefficients and very low nRMSEs
408 between the observed and modeled magnetic fields, resolves the geomagnetic field.

9. Conclusions

409 Produced in the near-equatorial region and controlled by the magnetic field in that
410 region, low-altitude isotropy boundaries have the potential to carry information about
411 field-line mapping and therefore could provide a suitable tool to probe the mapping accu-
412 racy of magnetospheric models. Using a suite of SWMF models for the magnetospheric
413 configuration we determined what is the strong scattering threshold condition based on
414 magnetic field solution from the MHD model and tested the conditions when the night-
415 side particle precipitation is dominated by field line curvature scattering of central plasma
416 sheet particles into the loss cone without including wave-particle interactions.

417 Magnetic field analysis based on data-model comparison reveals that the numerical sim-
418 ulation using the model setup presented here, reproduced in great detail the observations
419 from twelve different spacecraft, flying in the terrestrial magnetosphere during February
420 13, 2009. Therefore, based on the high correlation coefficients and very low nRMSEs
421 between the components of the observed and simulated magnetic field at the satellite
422 locations, we are confident that the model reproduces the magnetic field configuration
423 with high accuracy. Having a realistic representation of the magnetic field is imperative
424 since the scattering criterion, defined by the ratio between the radius of curvature and
425 the particle gyroradius, is a function of the magnitude of the total magnetic field and its
426 radius of curvature.

427 Our analysis predicts a $k = \frac{R_c}{\rho}$ ratio of ~ 33 . However, we presented here two represen-
428 tative examples of when observed isotropic boundaries were found on magnetic field lines
429 which crossed the equatorial plane at both low k and high k values. Our findings suggest
430 that, in the absence of other scattering mechanisms, the strong pitch angle scattering
431 could take place whenever the particle gyroradius is within two orders of magnitude of
432 the radius of curvature.

Acknowledgments. The authors would like to thank V. Sergeev for valuable discussions and suggestions. Work at University of Michigan was performed with financial support from the National Aeronautics and Space Administration grants NASA Award NNX14AF34G, NNX11A060G and NNX09AF45G and supported by the National Science Foundation under grant ATM-0802705. The work by N. Ganushkina and S. Dubyagin was also partly supported by the Academy of Finland and by the European Union Seventh Framework Programme (FP7/20072013) under grant agreements 606716 SPACESTORM and from the European Unions Horizon 2020 Research and Innovation Programme under grant agreement 637302 PROGRESS. The authors would like to thank the Kyoto World Data Center for the Dst index, and CDAWeb for allowing access to the plasma and magnetic field data. The NOAA/POES MEPED data are available at <http://satdat.ngdc.noaa.gov/sem/poes/data/full>. The data resulting from the numerical simulations are available upon request to the authors.

References

- Alexeev, I. I., V. V. Kalegaev, E. S. Belenkaya, S. Y. Bobrovnikov, Y. I. Feldstein, and L. I. Gromova, Dynamic model of the magnetosphere: Case study for January 9-12, 1997, *J. Geophys. Res.*, *106*, 25,683–25,694, doi:10.1029/2001JA900057, 2001.
- Asikainen, T., V. Maliniemi, and K. Mursula, Modeling the contributions of ring, tail, and magnetopause currents to the corrected Dst index, *Journal of Geophysical Research: Space Physics*, *115*(A), A12,203, 2010.
- Blockx, C., J. C. Gérard, M. Meurant, B. Hubert, and V. Coumans, Far ultraviolet remote sensing of the isotropy boundary and magnetotail stretching, *Journal of Geophysical*

- 454 *Research: Space Physics*, 110(A11), 2005.
- 455 Blockx, C., J. C. Gérard, V. Coumans, B. Hubert, and M. Meurant, A comparison be-
456 tween FUV remote sensing of magnetotail stretching and the T01 model during quiet
457 conditions and growth phases, *Annales Geophysicae*, 25(1), 161–170, 2007.
- 458 Braysy, T., K. Mursula, and G. Marklund, Ion cyclotron waves during a great magnetic
459 storm observed by Freja double-probe electric field instrument, *Journal of Geophysical*
460 *Research: Space Physics*, 103(A3), 4145–4155, 1998.
- 461 Buechner, J., and L. M. Zelenyi, Chaotization of the electron motion as the cause of an
462 internal magnetotail instability and substorm onset, *Journal of Geophysical Research*
463 (*ISSN 0148-0227*), 92(A12), 13,456–13,466, 1987.
- 464 De Zeeuw, D. L., S. Sazykin, R. A. Wolf, T. I. Gombosi, A. J. Ridley, and G. Toth,
465 Coupling of a global mhd code and an inner magnetospheric model: Initial results, *J.*
466 *Geophys. Res.*, 109, doi:10.1029/2003JA010,366, 2004.
- 467 Delcourt, D. C., J. A. Sauvaud, R. F. Martin, and T. E. Moore, On the nonadiabatic
468 precipitation of ions from the near-Earth plasma sheet, *Journal of Geophysical Research*,
469 101(A), 17,409–17,418, 1996.
- 470 Donovan, E., B. Jackel, D. Klumpar, and R. Strangeway, Energy dependence of the
471 isotropy boundary latitude, in *Proc. of Atmos. Studies by Optical Methods*, vol. 92, pp.
472 11–14, 2003a.
- 473 Donovan, E. F., B. J. Jackel, I. Voronkov, T. Sotirelis, F. Creutzberg, and N. A. Nicholson,
474 Ground-based optical determination of the b2i boundary: A basis for an optical MT-
475 index, *Journal of Geophysical Research: Space Physics*, 108(A), 1115, 2003b.

- 476 Dubyagin, S., N. Ganushkina, S. Apatenkov, M. Kubyshkina, H. Singer, and M. Liemohn,
477 Geometry of duskside equatorial current during magnetic storm main phase as deduced
478 from magnetospheric and low-altitude observations, *Annales Geophysicae*, *31*(3), 395–
479 408, 2013.
- 480 Erlandson, R. E., and A. J. Ukhorskiy, Observations of electromagnetic ion cyclotron
481 waves during geomagnetic storms: Wave occurrence and pitch angle scattering, *Journal*
482 *of Geophysical Research: Space Physics*, *106*(A3), 3883–3895, 2001.
- 483 Fritz, T. A., Study of the high-latitude, outer-zone boundary region for ≥ 40 -keV electrons
484 with satellite Injun 3, *Journal of Geophysical Research: Space Physics (1978–2012)*,
485 *75*(28), 5387–5400, 1970.
- 486 Ganushkina, N., T. Pulkkinen, M. Kubyshkina, H. Singer, and C. Russell, Long-term
487 evolution of magnetospheric current systems during storms, *Annales Geophysicae*, *22*,
488 1317–1334, doi:10.5194/angeo-22-1317-2004, 2004.
- 489 Ganushkina, N. Y., T. I. Pulkkinen, M. V. Kubyshkina, V. A. Sergeev, E. A. Lvova, T. A.
490 Yahnina, A. G. Yahnin, and T. Fritz, Proton isotropy boundaries as measured on mid-
491 and low-altitude satellites, *Annales Geophysicae*, *23*(5), 1839–1847, 2005.
- 492 Ganushkina, N. Y., M. W. Liemohn, M. V. Kubyshkina, R. Ilie, and H. J. Singer, Dis-
493 tortions of the magnetic field by storm-time current systems in Earth’s magnetosphere,
494 *Annales Geophysicae*, *28*, 123–140, doi:10.5194/angeo-28-123-2010, 2010.
- 495 Gilson, M. L., J. Raeder, E. Donovan, Y. S. Ge, and S. B. Mende, Statistics of the longi-
496 tudinal splitting of proton aurora during substorms, *Journal of Geophysical Research*,
497 *116*(A), A08,226, 2011.

- 498 Gilson, M. L., J. Raeder, E. Donovan, Y. S. Ge, and L. Kepko, Global simulation of
499 proton precipitation due to field line curvature during substorms, *Journal of Geophysical*
500 *Research: Space Physics*, 117(A), 2012.
- 501 Glocer, A., G. Tóth, Y. Ma, T. Gombosi, J.-C. Zhang, and L. M. Kistler, Multifluid Block-
502 Adaptive-Tree Solar wind Roe-type Upwind Scheme: Magnetospheric composition and
503 dynamics during geomagnetic storms:Initial results, *Journal of Geophysical Research*
504 (*Space Physics*), 114(A13), A12203, doi:10.1029/2009JA014418, 2009.
- 505 Gombosi, T. I., G. Tóth, D. L. De Zeeuw, K. C. Hansen, K. Kabin, and K. G. Powell,
506 Semirelativistic Magnetohydrodynamics and Physics-Based Convergence Acceleration,
507 *Journal of Computational Physics*, 177, 176–205, doi:10.1006/jcph.2002.7009, 2002.
- 508 Halford, A. J., B. J. Fraser, and S. K. Morley, EMIC wave activity during geomagnetic
509 storm and nonstorm periods: CRRES results, *Journal of Geophysical Research: Space*
510 *Physics*, 115(A), 2010.
- 511 Harel, M., R. A. Wolf, P. H. Reiff, R. W. Spiro, W. J. Burke, F. J. Rich, and M. Smiddy,
512 Quantitative simulation of a magnetospheric substorm. I - Model logic and overview,
513 *J. Geophys. Res.*, 86, 2217–2241, doi:10.1029/JA086iA04p02217, 1981.
- 514 Hultqvist, B., The hot ion component of the magnetospheric plasma and some relations
515 to the electron component - Observations and physical implications, *Space Science Re-*
516 *views*, 23(4), 581–675, 1979.
- 517 Ilie, R., M. W. Liemohn, J. Borovsky, and J. Kozyra, An investigation of the
518 magnetosphere-ionosphere response to real and idealized CIR events through global
519 MHD simulations, *Proceedings to Royal Society A*, doi:doi:10.1098/rspa.2010.0074,
520 2010a.

- 521 Ilie, R., M. W. Liemohn, and A. Ridley, The effect of smoothed solar wind inputs on
522 global modeling results, *J. Geophys. Res.*, *115*, doi:10.1029/2009JA014443, 2010b.
- 523 Ilie, R., R. M. Skoug, P. Valek, H. O. Funsten, and A. Glocer, Global view of inner
524 magnetosphere composition during storm time, *Journal of Geophysical Research: Space*
525 *Physics*, *118*(1), 7074–7084, 2013.
- 526 Ilie, R., M. W. Liemohn, G. Toth, N. Yu Ganushkina, and L. K. S. Daldorff, Assess-
527 ing the role of oxygen on ring current formation and evolution through numerical ex-
528 periments, *Journal of Geophysical Research: Space Physics*, *120*(6), 4656–4668, doi:
529 10.1002/2015JA021157, 2015JA021157, 2015.
- 530 Kubyshkina, M., V. Sergeev, N. Tsyganenko, V. Angelopoulos, A. Runov, H. Singer, K. H.
531 Glassmeier, H. U. Auster, and W. Baumjohann, Toward adapted time-dependent mag-
532 netospheric models: A simple approach based on tuning the standard model, *Journal*
533 *of Geophysical Research*, *114*(A), A00C21, 2009.
- 534 Liemohn, M. W., D. L. De Zeeuw, R. Ilie, and N. Y. Ganushkina, Decipher-
535 ing magnetospheric cross-field currents, *Geophys. Res. Lett.*, *38*, L20106, doi:
536 10.1029/2011GL049611, 2011.
- 537 Lvova, E. A., V. A. Sergeev, and G. R. Bagautdinova, Statistical study of the proton
538 isotropy boundary, *Annales Geophysicae*, *23*(4), 1311–1316, 2005.
- 539 Meng, X., G. Tóth, M. W. Liemohn, T. I. Gombosi, and A. Runov, Pressure anisotropy
540 in global magnetospheric simulations: A magnetohydrodynamics model, *Journal of*
541 *Geophysical Research: Space Physics*, *117*(A), A08,216, 2012.
- 542 Meurant, M., J. C. Gérard, C. Blockx, E. Spanswick, E. F. Donovan, B. Hubert,
543 V. Coumans, and M. Connors, EL - a possible indicator to monitor the magnetic field

- 544 stretching at global scale during substorm expansive phase: Statistical study, *Journal*
545 *of Geophysical Research: Space Physics*, *112*(A), A05,222, 2007.
- 546 Powell, K. G., P. L. Roe, T. J. Linde, T. I. Gombosi, and D. L. De Zeeuw, A Solution-
547 Adaptive Upwind Scheme for Ideal Magnetohydrodynamics, *Journal of Computational*
548 *Physics*, *154*, 284–309, doi:10.1006/jcph.1999.6299, 1999.
- 549 Ridley, A., T. Gombosi, and D. Dezeeuw, Ionospheric control of the magnetosphere:
550 conductance, *Annales Geophysicae*, *22*, 567–584, 2004.
- 551 Ridley, A. J., and M. W. Liemohn, A model-derived storm time asymmetric ring current
552 driven electric field description, *Journal of Geophysical Research (Space Physics)*, *107*,
553 1151–+, doi:10.1029/2001JA000051, 2002.
- 554 Sandel, B. R., et al., The Extreme Ultraviolet Imager Investigation for the IMAGE Mis-
555 sion, *Space Science Reviews*, *91*(1), 197–242, 2000.
- 556 Sergeev, V. A., and B. B. Gvozdevsky, Mt-index: a possible new index to characterize
557 the magnetic configuration of magnetotail, *Annales Geophysicae*, *13*(10), 1093–1103,
558 doi:10.1007/s00585-995-1093-9, 1995.
- 559 Sergeev, V. A., and N. A. Tsyganenko, Energetic Particle Losses and Trapping Boundaries
560 as Deduced From Calculations with a Realistic Magnetic-Field Model, *Planetary and*
561 *Space Science*, *30*(10), 999–1006, 1982.
- 562 Sergeev, V. A., E. M. SAZHINA, N. A. Tsyganenko, J. A. LUNDBLAD, and F. SO-
563 RAAS, Pitch-Angle Scattering of Energetic Protons in the Magnetotail Current Sheet
564 as the Dominant Source of Their Isotropic Precipitation Into the Nightside Ionosphere,
565 *Planetary and Space Science*, *31*(10), 1147–1155, 1983.

- 566 Sergeev, V. A., M. Malkov, and K. Mursula, Testing the isotropic boundary algorithm
567 method to evaluate the magnetic field configuration in the tail, *Journal of Geophysical*
568 *Research (ISSN 0148-0227)*, 98(A5), 7609–7620, 1993.
- 569 Sergeev, V. A., T. I. Pulkkinen, T. I. Pellinen, and N. A. Tsyganenko, Hybrid state of
570 the tail magnetic configuration during steady convection events, *Journal of Geophysical*
571 *Research (ISSN 0148-0227)*, 99(A12), 23,571–23,582, 1994.
- 572 Sergeev, V. A., S. A. Chernyaeva, S. V. Apatenkov, N. Y. Ganushkina, and S. V. Dubya-
573 gin, Energy-latitude dispersion patterns near the isotropy boundaries of energetic pro-
574 tons, *Annales Geophysicae*, doi:in press, 2015.
- 575 Toffoletto, F., S. Sazykin, R. Spiro, and R. Wolf, Inner magnetospheric model-
576 ing with the Rice Convection Model, *Space Science Reviews*, 107, 175–196, doi:
577 10.1023/A:1025532008047, 2003.
- 578 Tóth, G., Y. Ma, and T. I. Gombosi, Hall magnetohydrodynamics on block-adaptive grids,
579 *Journal of Computational Physics*, 227, 6967–6984, doi:10.1016/j.jcp.2008.04.010, 2008.
- 580 Tóth, G., et al., Space Weather Modeling Framework: A new tool for the space science
581 community, *Journal of Geophysical Research (Space Physics)*, 110(A9), 12,226–+, doi:
582 10.1029/2005JA011126, 2005.
- 583 Tóth, G., et al., Adaptive numerical algorithms in space weather modeling, *Journal of*
584 *Computational Physics*, 231, 870–903, doi:10.1016/j.jcp.2011.02.006, 2012.
- 585 Tsyganenko, N. A., Pitch-Angle Scattering of Energetic Particles in the Current Sheet of
586 the Magnetospheric Tail and Stationary Distribution-Functions, *Planetary and Space*
587 *Science*, 30(5), 433–437, 1982.

- 588 Tsyganenko, N. A., Modeling the Earth's magnetospheric magnetic field confined within
589 a realistic magnetopause, *J. Geophys. Res.*, *100*, 5599–5612, doi:10.1029/94JA03193,
590 1995.
- 591 Tsyganenko, N. A., A model of the near magnetosphere with a dawn-dusk asymmetry 1.
592 Mathematical structure, *Journal of Geophysical Research (Space Physics)*, *107*, 1179–+,
593 doi:10.1029/2001JA000219, 2002.
- 594 Tsyganenko, N. A., and M. I. Sitnov, Modeling the dynamics of the inner magnetosphere
595 during strong geomagnetic storms, *Journal of Geophysical Research (Space Physics)*,
596 *110*, A03208, doi:10.1029/2004JA010798, 2005.
- 597 Usanova, M. E., I. R. Mann, J. Bortnik, L. Shao, and V. Angelopoulos, THEMIS obser-
598 vations of electromagnetic ion cyclotron wave occurrence: Dependence on AE, SYMH,
599 and solar wind dynamic pressure, *Journal of Geophysical Research*, *117*(A), A10,218,
600 2012.
- 601 Welling, D. T., and M. W. Liemohn, Outflow in global magnetohydrodynamics as a
602 function of a passive inner boundary source, *Journal of Geophysical Research: Space
603 Physics*, *119*(4), 2691–2705, 2014.
- 604 Yahnin, A. G., and T. A. Yahnina, Energetic proton precipitation related to ion-cyclotron
605 waves, *Journal of Atmospheric and Solar-Terrestrial Physics*, *69*(14), 1690–1706, 2007.
- 606 Yu, Y., and A. J. Ridley, Response of the magnetosphere-ionosphere system to a sudden
607 southward turning of interplanetary magnetic field, *Journal of Geophysical Research
608 (Space Physics)*, *114*(A13), 3216–+, doi:10.1029/2008JA013292, 2009.
- 609 Zhang, J., et al., Solar and interplanetary sources of major geomagnetic storms during
610 1996-2005, *Journal of Geophysical Research (Space Physics)*, *112*(A11), 10,102–+, doi:

Figure 1. February 13, 2009 event parameters. Panel **a** present all components of the interplanetary magnetic field (B_x green line, B_y blue line, B_z red line, B magnitude (black line)). Panel **b** shows the solar wind number density (black line) and temperature (blue line). Panel **c** presents all components of the solar wind velocity (V_x green line, V_y blue line, V_z red line) followed the electric field (red line) and CPCP Index (black line) in panel **d**. The bottom panel (n panel **e**) presents Sym-H index throughout this period.

⁶¹¹ 10.1029/2007JA012321, 2007.

Author Manuscript

Spacecraft/Time	Plane	k	B_{min} (nT)	$X(R_e)$	$Y(R_e)$	$Z(R_e)$	$R_c(R_e)$	Conj. with
METOP-02/01:41:16	Minimum B	38.45	71.45	-6.71	2.10	-2.07	2.12	THEMIS A, D
METOP-02/01:41:16	SM Z=0	38.44	72.94	-6.57	2.11	-2.45	2.18	THEMIS A, D
METOP-02/03:22:00	Minimum B	39.00	75.60	-6.53	-0.26	-2.24	2.03	THEMIS A, D, E
METOP-02/03:22:00	SM Z=0	39.03	75.90	-6.47	-0.27	-2.79	2.04	THEMIS A, D, E
NOAA-16/02:23:16	Minimum B	30.71	64.59	-6.89	-0.15	-2.45	1.91	THEMIS A, D, E
NOAA-16/02:23:16	SM Z=0	30.70	63.01	-6.78	-0.13	-2.72	1.97	THEMIS A, D, E
NOAA-16/02:25:23	Minimum B	27.62	56.70	-6.80	2.02	-2.38	1.91	THEMIS A, E
NOAA-16/02:25:23	SM Z=0	27.62	56.69	-6.67	2.03	-2.68	2.00	THEMIS A, E
NOAA-17/02:41:34	Minimum B	28.49	58.96	-6.86	0.72	-2.54	1.90	THEMIS A, D, E
NOAA-17/02:41:34	SM Z=0	28.48	59.88	-6.75	0.73	-2.78	1.96	THEMIS A, D, E
NOAA-17/04:22:02	Minimum B	44.10	80.97	-6.29	-1.79	-2.70	2.14	THEMIS A, E
NOAA-17/04:22:02	SM Z=0	44.10	81.10	-6.24	-1.79	-2.80	2.15	THEMIS A, E
NOAA-18/16:54:17	Minimum B	43.80	88.18	-5.39	-4.21	-0.11	1.95	THEMIS A, E
NOAA-18/16:54:17	SM Z=0	43.80	88.31	-5.38	-4.21	-0.21	1.96	THEMIS A, E

Table 1. THEMIS and NOAA conjugacies for isotropic boundaries observations during the February 13, 2009 period.

Author Manuscript

Figure 2. Locations of isotropic boundaries during February 13, 2009 observed by all available NOAA-POES satellites as a function of magnetic latitude (a) and magnetic local time (b).

Author Manuscript

Figure 3. Coupling schematic of the model couplings within SWMF.

D R A F T

December 10, 2015, 8:09am

D R A F T

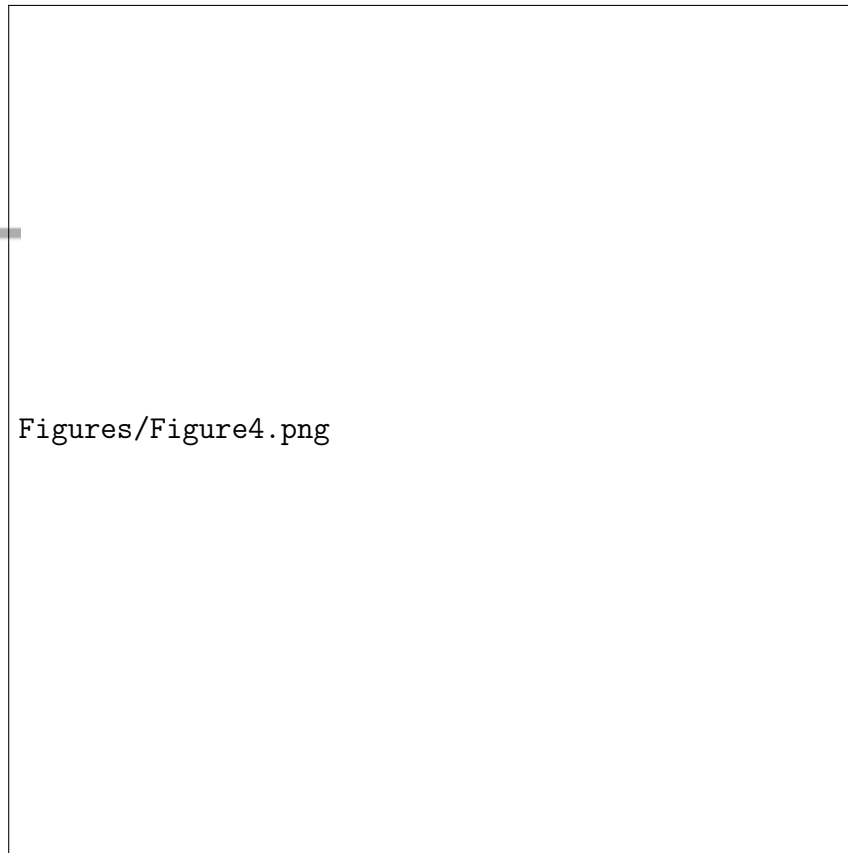


Figure 4. Comparison between the total magnetic field as output from SWMF magnetospheric modeling (red) and observed at GOES 11 (black) for February 13, 2009 interval. Top row shows the spacecraft position in the $Y, Z = 0$ planes, followed the magnetic field components as measured by the satellite (black lines) and predicted by the model (red lines). The green diamond, star, and triangle are used to show the satellite position and progression during the time interval presented here. Correlation coefficients between the observed and simulated values of B_x , B_y , B_z are indicated in each of the corresponding panels.

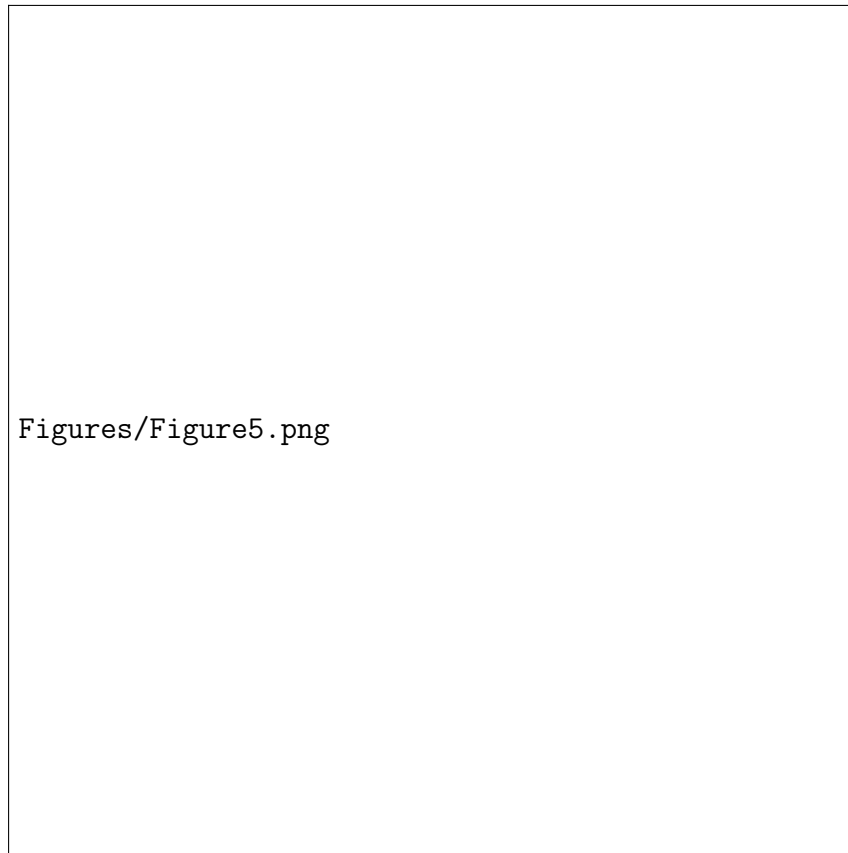


Figure 5. Comparison between the total magnetic field as output from SWMF magnetospheric modeling (red) and observed at Geotail (black) for February 13, 2009 interval. Top row shows the spacecraft position in the $Y, Z = 0$ planes, followed the magnetic field components as measured by the satellite (black lines) and predicted by the model (red lines). The green diamond, star, and triangle are used to show the satellite position and progression during the time interval presented here. Correlation coefficients between the observed and simulated values of B_x , B_y , B_z are indicated in each of the corresponding panels.

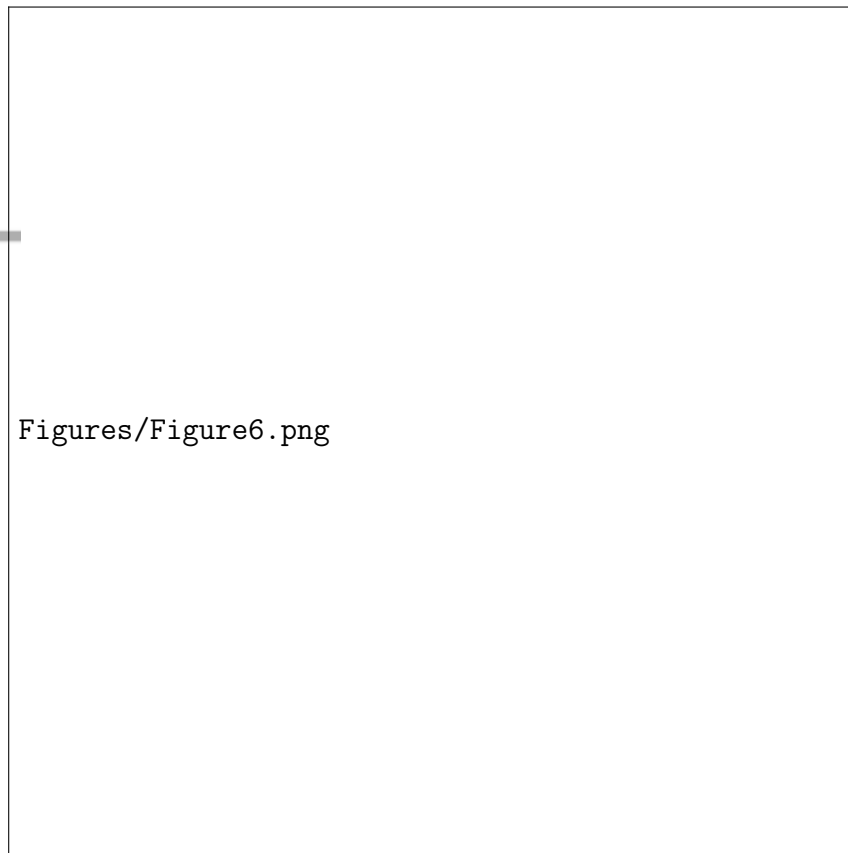


Figure 6. Comparison between the total magnetic field as output from SWMF magnetospheric modeling (red) and observed at THEMIS-A (black) for February 13, 2009 interval. Top row shows the spacecraft position in the $Y, Z = 0$ planes, followed the magnetic field components as measured by the satellite (black lines) and predicted by the model (red lines). The green diamond, star, and triangle are used to show the satellite position and progression during the time interval presented here. Correlation coefficients between the observed and simulated values of B_x, B_y, B_z are indicated in each of the corresponding panels.

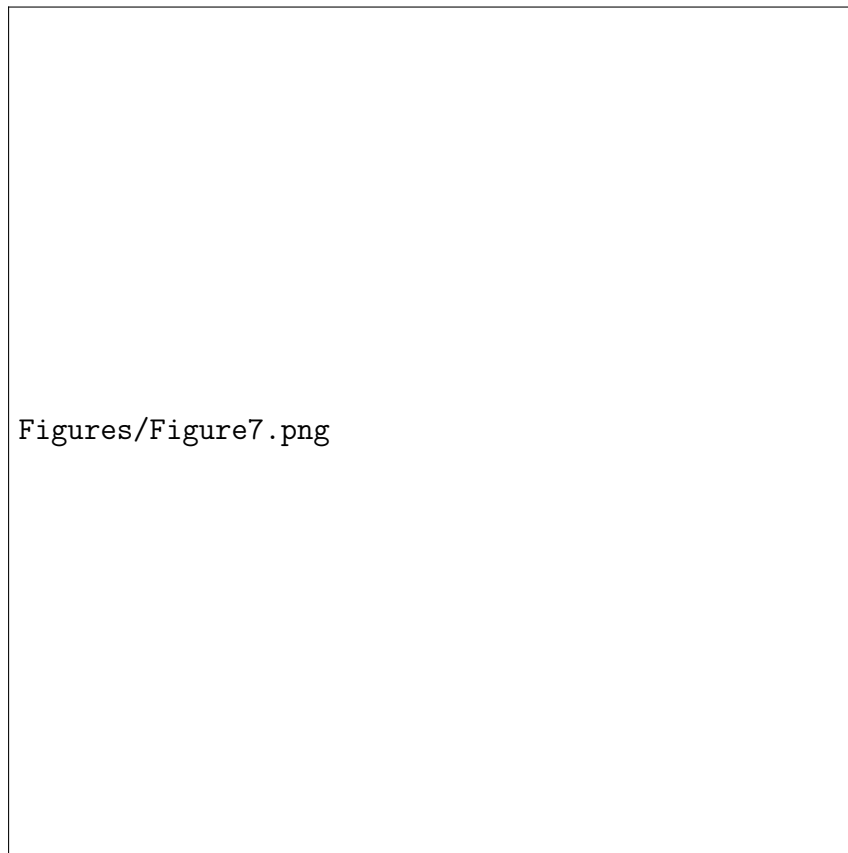


Figure 7. Comparison between the total magnetic field as output from SWMF magnetospheric modeling (red) and observed at THEMIS-C (black) for February 13, 2009 interval. Top row shows the spacecraft position in the $Y, Z = 0$ planes, followed the magnetic field components as measured by the satellite (black lines) and predicted by the model (red lines). The green diamond, star, and triangle are used to show the satellite position and progression during the time interval presented here. Correlation coefficients between the observed and simulated values of B_x, B_y, B_z are indicated in each of the corresponding panels.

Author Manuscript

Figure 8. Magnetic field strength on the minimum \mathbf{B} surface (left panel) and SM $z = 0$ plane (right panel). The scale is logarithmic. A field line is traced from the location of NOAA 18 satellite 0403 UT in the simulation.

Author Manuscript

Figure 9. Comparative view of the values of $k = \frac{Rc}{\rho}$ ratio for a 30 keV energy ion calculated on the minimum \mathbf{B} surface (left panel) and SM $z = 0$ plane (right panel). The color scale is saturated at values of $k = 10$. A field line is traced from the location of NOAA 18 satellite 0403 UT in the simulation.

D R A F T

December 10, 2015, 8:09am

D R A F T

Author Manuscript

Figure 10. Comparative view of the values of $k = \frac{Rc}{\rho}$ ratio for a 30 keV energy ion calculated on the minimum \mathbf{B} surface (left panel) and SM $z = 0$ plane (right panel). The color scale is saturated at values of $k = 10$. A field line is traced from the location of NOAA 17 satellite 1257 UT in the simulation.

D R A F T

December 10, 2015, 8:09am

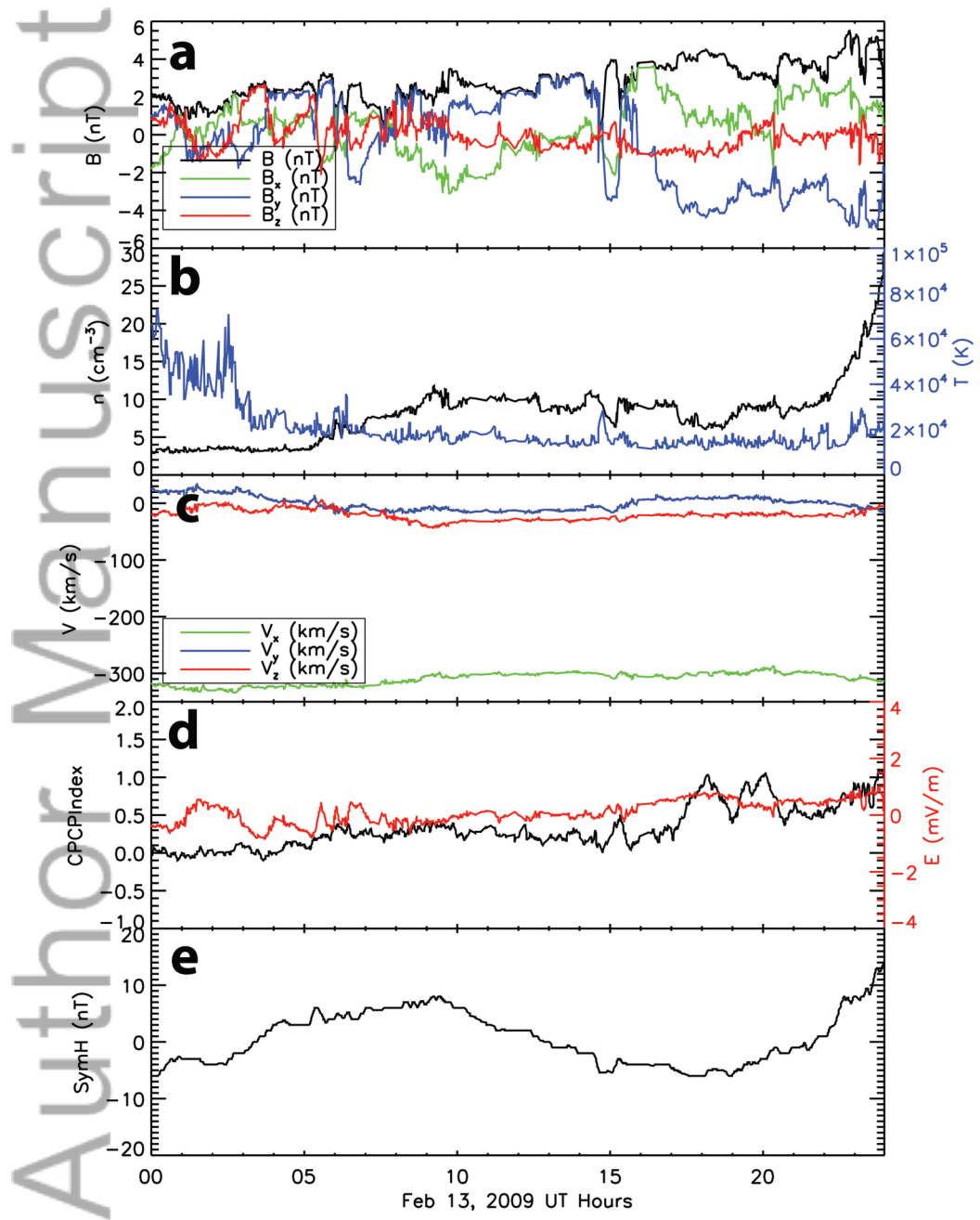
D R A F T

Table 2. Normalized root mean square errors (nRMSE) and Correlation coefficients (R)

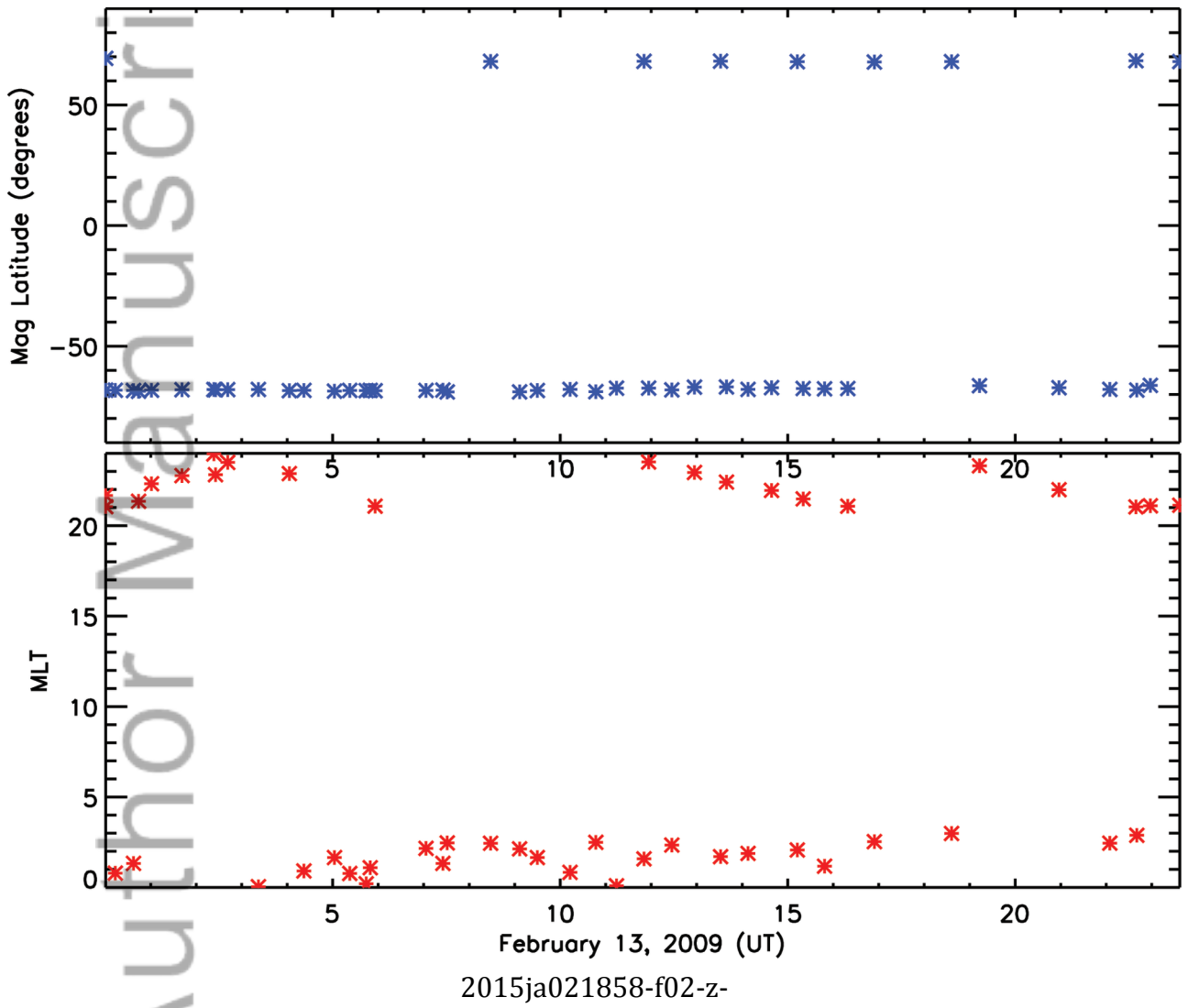
between the simulated and observed magnetic field values.

SPACECRAFT	nRMSE(B_x)	nRMSE(B_y)	nRMSE(B_z)	R(B_x)	R(B_y)	R(B_z)
Cluster 1	0.0064	0.0131	0.0087	0.890	0.929	0.809
Cluster 2	0.0061	0.0162	0.0087	0.873	0.890	0.802
Cluster 3	0.0013	0.0163	0.0048	0.700	0.860	0.782
Cluster 4	0.0071	0.0134	0.0094	0.877	0.905	0.809
Geotail	0.0815	0.0808	0.1397	0.985	0.934	0.952
GOES 11	0.0820	0.1136	0.0909	0.977	0.983	0.885
GOES 12	0.0538	0.0375	0.3083	0.994	0.995	0.713
THEMIS-A	0.0073	0.0084	0.0095	0.923	0.921	0.970
THEMIS-B	0.1994	0.1091	0.1340	0.736	0.738	0.444
THEMIS-C	0.1190	0.0679	0.1192	0.926	0.774	0.708
THEMIS-D	0.0157	0.0188	0.0122	0.962	0.881	0.965
THEMIS-E	0.0086	0.0108	0.0095	0.961	0.959	0.967

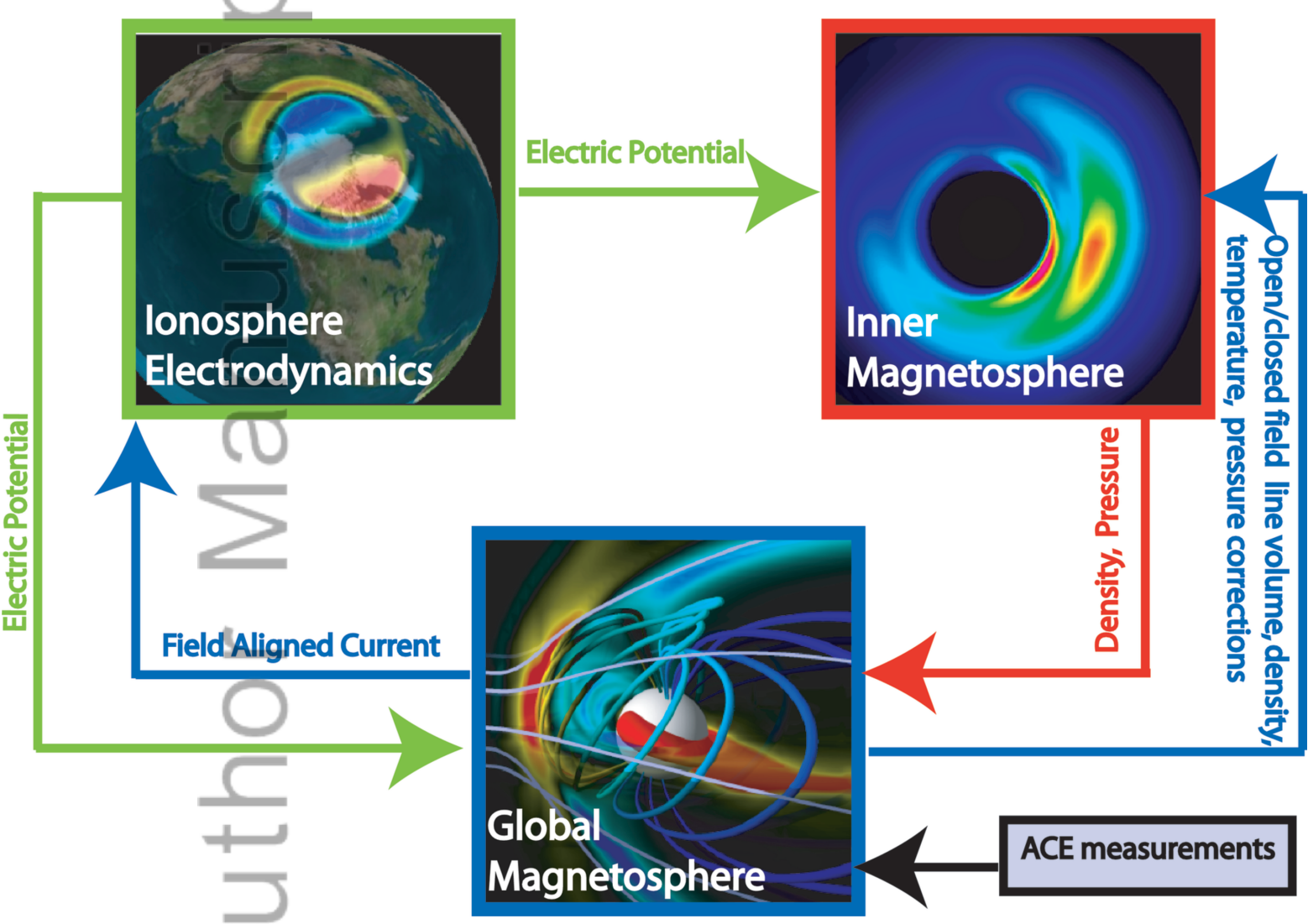
Figure 11. $k = \frac{Rc}{\rho}$ versus $\Delta B = \frac{B^{modeled} - B^{observed}}{B^{observed}}$ on the nightside ($0300 < MLT < 2100$) for February 13th, 2009 quiet time period. The red line represents the linear fit $k = 32.95\Delta B + 17.5$.



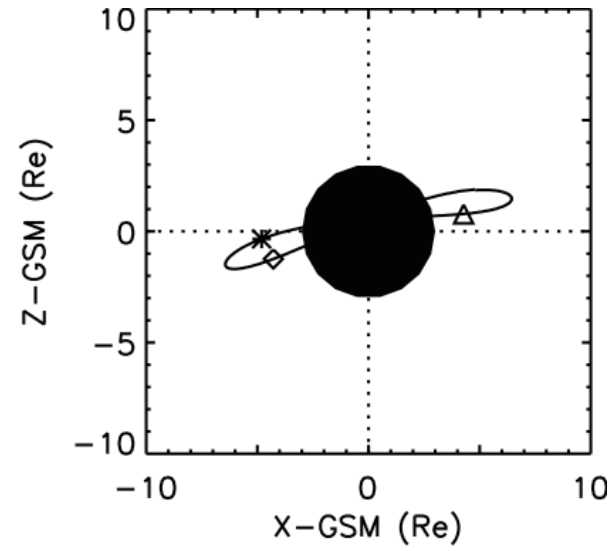
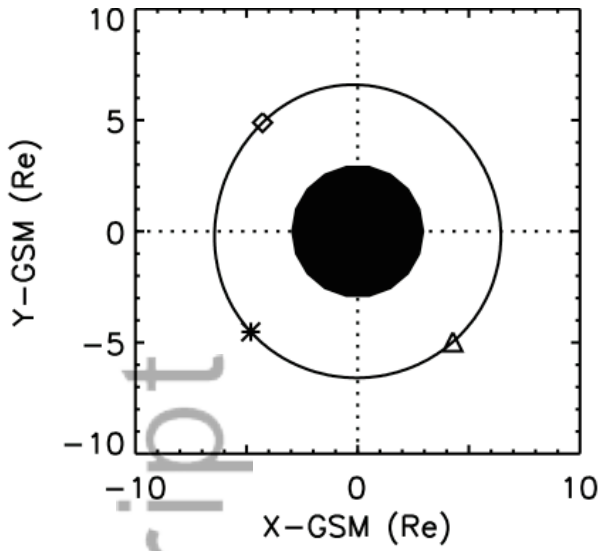
2015ja021858-f01-z-



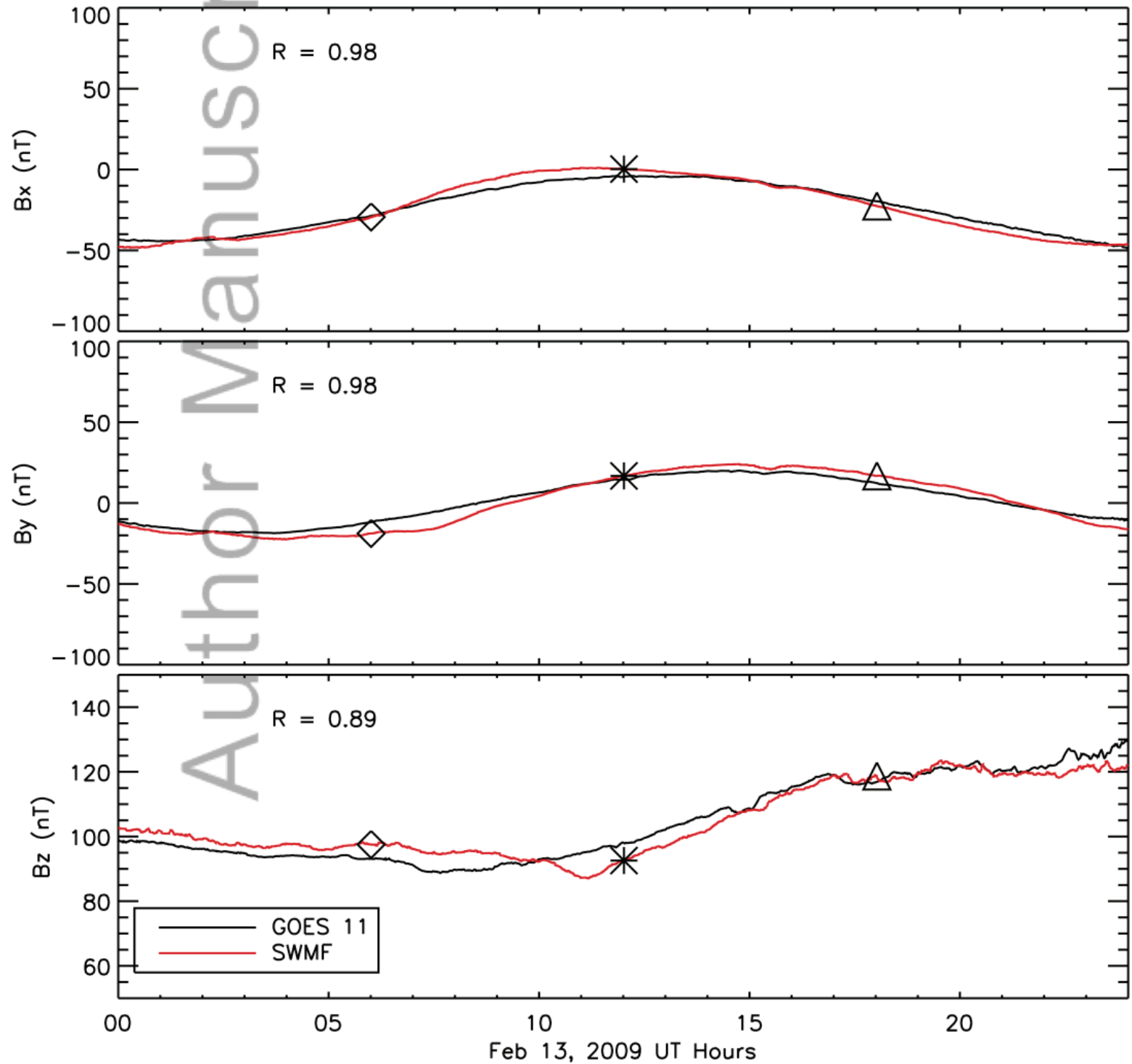
Author Manuscript

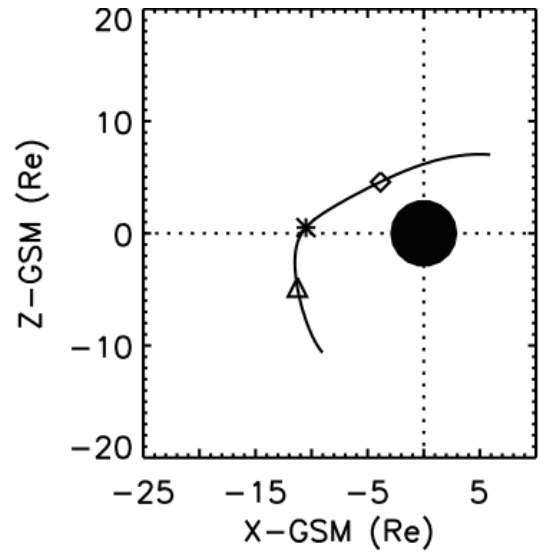
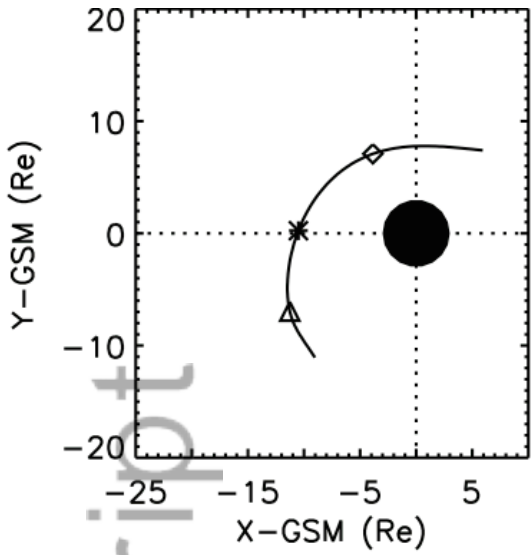


2015ja021858-f03-z-

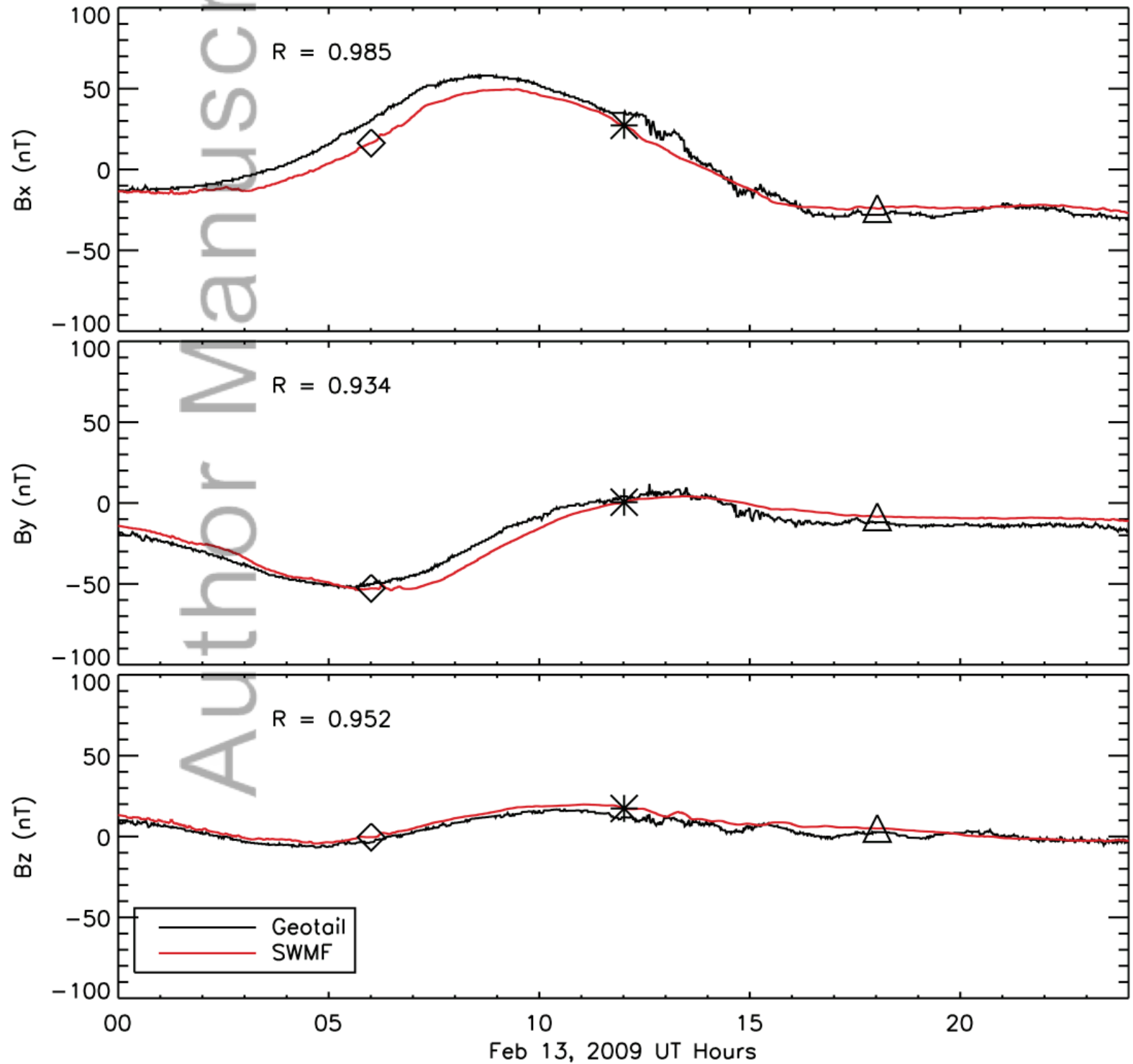


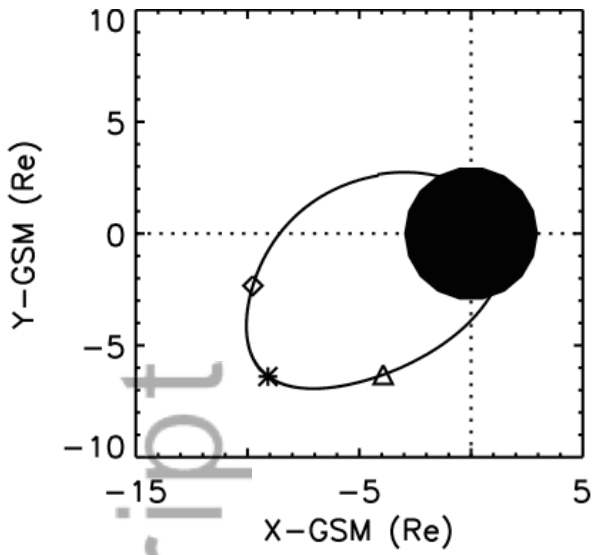
GOES 11



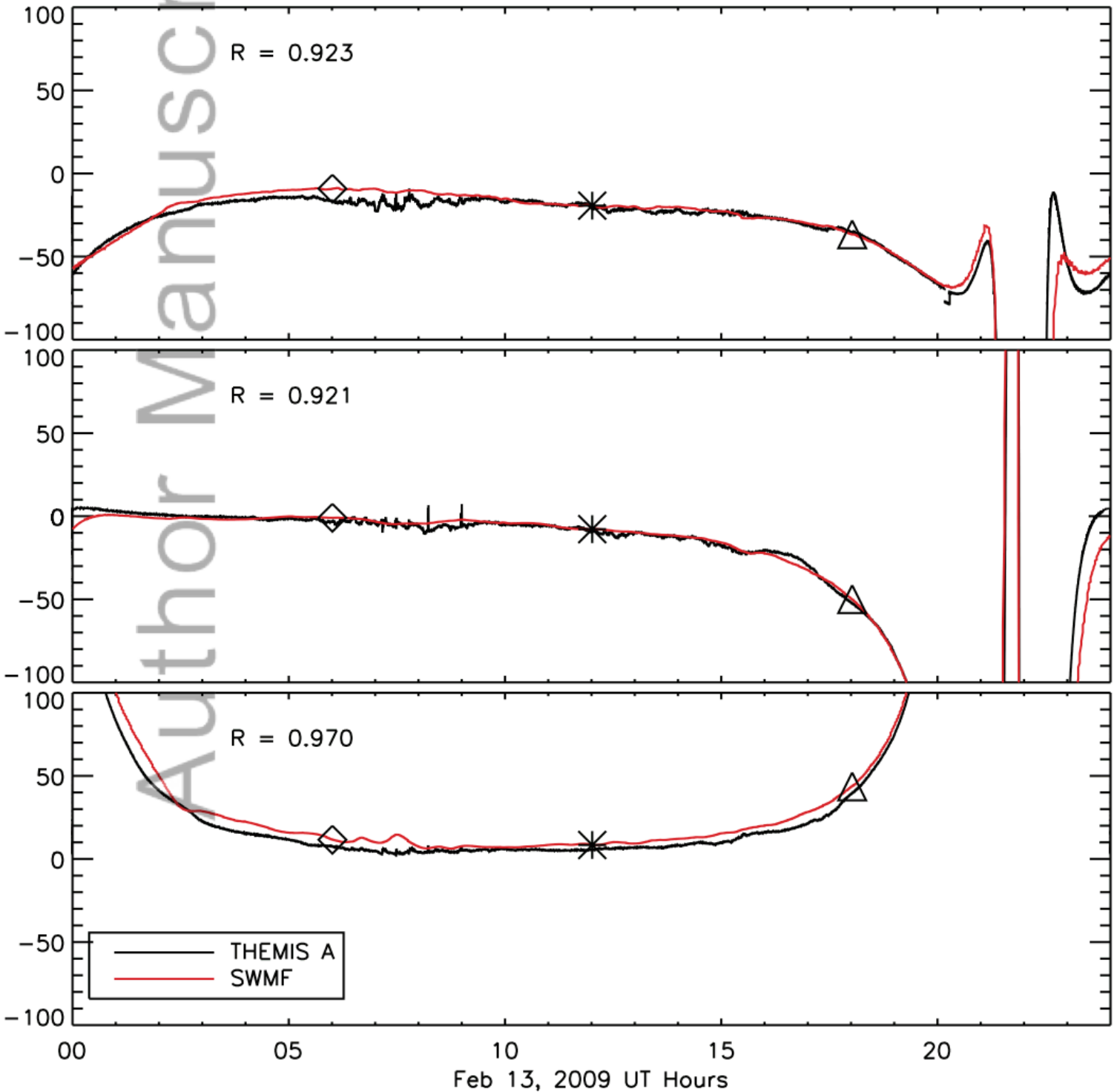
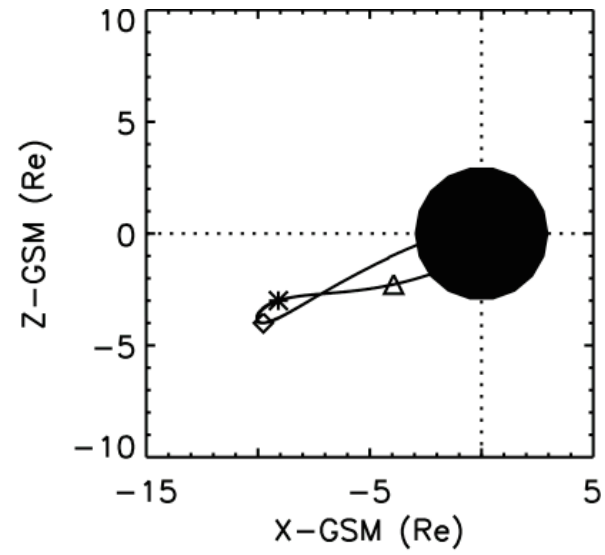


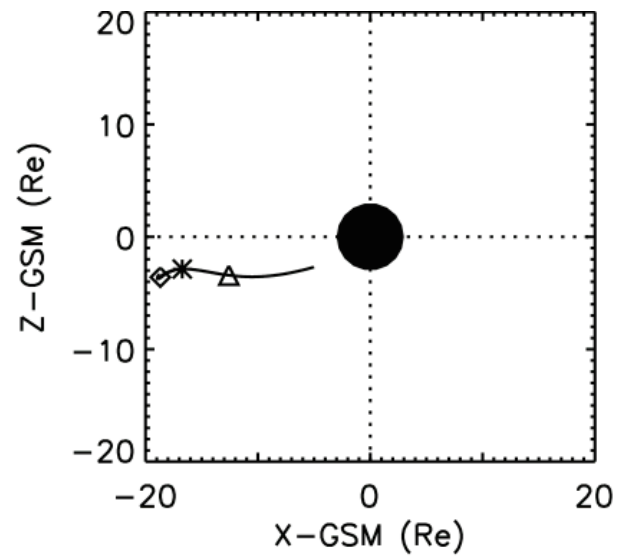
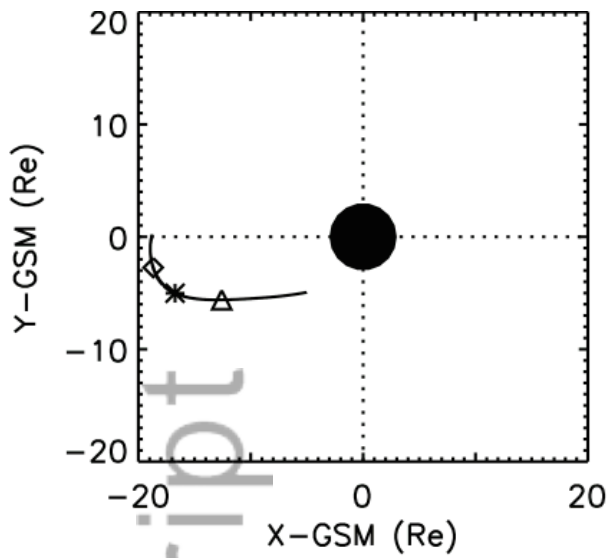
Geotail



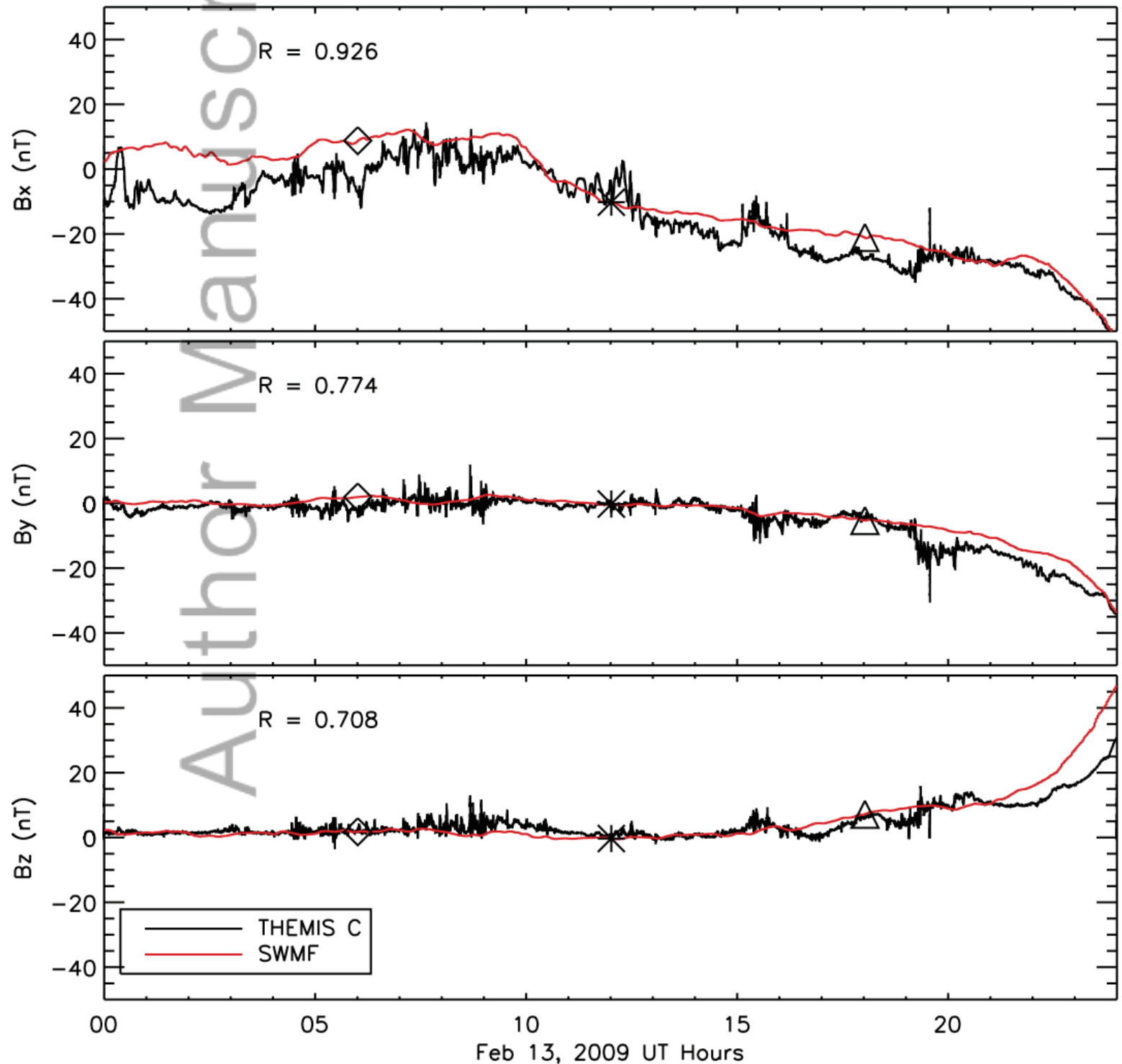


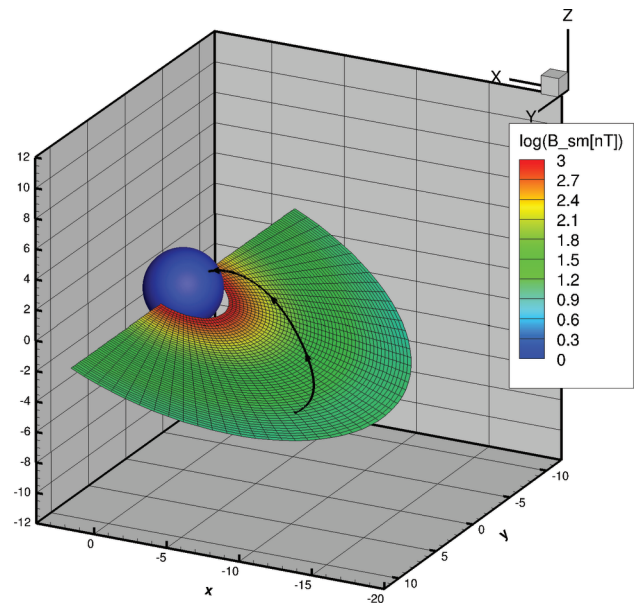
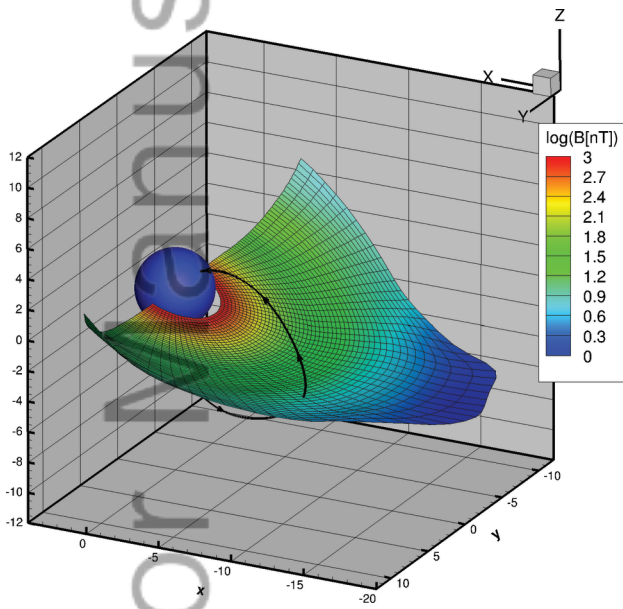
THEMIS A



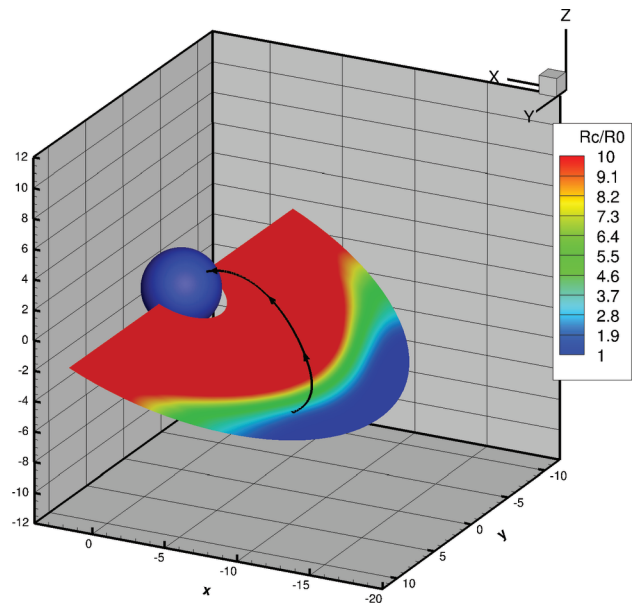
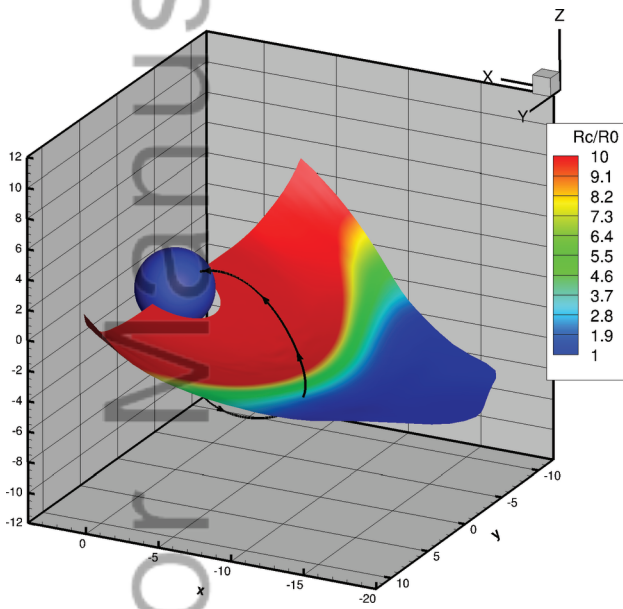


THEMIS C

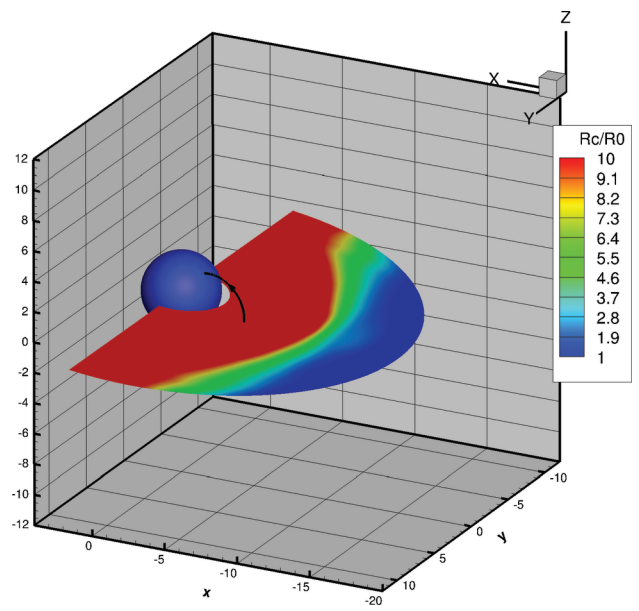
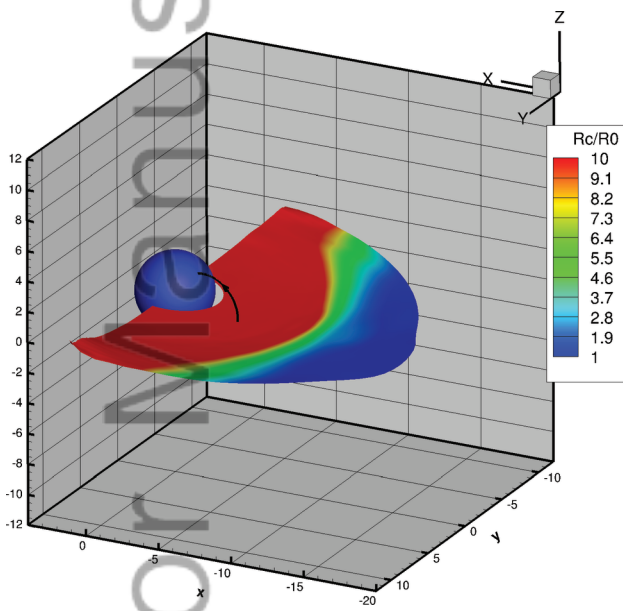




2015ja021858-f08-z-



2015ja021858-f09-z-



2015ja021858-f10-z-

